TopoEliashberg

Quantum-Geometry-Guided First-Principles Discovery of Electrically Switchable Majorana Phases in Altermagnetic Heterostructures

From Quantum ESPRESSO Electron-Phonon Calculations to Material-Resolved Bogoliubov-de Gennes Topology

Rihaan Shah

July 18, 2026

Abstract

Topological-superconductor screening is often performed by taking a first-principles normal-state Hamiltonian and adding a constant pairing parameter by hand. That approximation is useful for intuition, but it suppresses the central materials question: whether the electronic states that carry strong spin-orbit texture, Berry curvature, or band inversion are also the states that receive a sufficiently large superconducting gap. This paper develops *TopoEliashberg*, a publication-style computational framework that connects relaxed layered crystal structures, noncollinear spin-orbit density-functional theory, density-functional perturbation theory, Wannier interpolation, anisotropic Migdal-Eliashberg superconductivity, material-resolved Bogoliubov-de Gennes topology, and finite-device Majorana diagnostics. Quantum ESPRESSO is assigned the first-principles tasks it can directly perform: structural relaxation, magnetic energetics, Berry-phase polarization, spin-orbit electronic structure, phonons, and electron-phonon matrix elements. Wannier90 and EPW supply the spinor tight-binding representation and the superconducting pairing data. Downstream BdG, Green-function, real-space, and transport calculations then test superconducting topology and boundary localization.

The methodological center is an explicit transfer of a band- and momentum-dependent gap $\Delta_n(\mathbf{k}, T)$ into an orbital-spin Wannier pairing matrix $\Delta_{\alpha\beta}(\mathbf{k}, T)$ with gauge, degeneracy, and fermionic-antisymmetry checks. We introduce an Eliashberg-Topology Overlap (ETO) and quantum-geometric extensions as screening descriptors that weight Berry curvature, quantum metric, and spin texture by the material-derived superconducting gap on the Fermi surface. The primary case-study architecture is a CrSBr-like van der Waals altermagnetic layer, a sliding-hBN-like polar control interface, and an $NbSe_2$-like electron-phonon superconductor. All numerical phase diagrams and finite-device figures in this manuscript are explicitly labeled as controlled synthetic or model-generated demonstrations; no unperformed Quantum ESPRESSO, EPW, Wannier90, or transport calculation is presented as a completed first-principles prediction. The result is a rigorous roadmap and benchmark paper for deciding when realistic pairing changes superconducting topological phase boundaries, minigaps, Majorana localization lengths, and disorder thresholds.

Claim-status legend. Each result is labeled as directly generated in this package, analytically derived, reproduced from published literature, a synthetic/model demonstration, or a proposed future first-principles calculation. The present package directly generates the LaTeX source, BibTeX file, vector figures, input templates, and a compiled PDF. It does not execute material-specific QE/EPW production calculations.

Contents

1 Introduction

The central problem in computational Majorana materials design is not merely to find a normal-state band inversion. A normal-state Chern number, a Berry-curvature hot spot, or a visually appealing edge state does not by itself establish topological superconductivity. A superconducting topological phase is a property of a Bogoliubov-de Gennes Hamiltonian, so it depends on particle-hole doubling, the pairing matrix, the chemical potential, broken and preserved symmetries, and the stability of the quasiparticle gap. The same normal-state band structure may therefore be trivial or topological depending on which orbitals are paired, how strongly they are paired, whether the pairing changes sign across the Fermi surface, and whether disorder or temperature closes the topological minigap.

First-principles workflows for topological materials have become highly mature. Quantum ESPRESSO can perform plane-wave DFT, noncollinear spin-orbit calculations, Berry-phase polarization calculations, phonons, and electron-phonon calculations through EPW and related tools [1–5]. Wannier90 can construct spinor tight-binding models and evaluate Berry-phase quantities on dense meshes [6–8]. EPW implements Wannier-interpolated electron-phonon coupling and anisotropic Migdal-Eliashberg calculations [9–11]. What is still uncommon is an auditable interface that carries the *material-derived, momentum-resolved pairing function* into a topological BdG calculation without collapsing it into a scalar Δ_0.

Altermagnets sharpen this need. They provide compensated magnetic order with momentum-dependent spin splitting and little or no net magnetization, a setting that can imitate useful time-reversal breaking without the large stray fields of ferromagnets [12–14]. Recent theory has already proposed altermagnetic routes to Majorana modes [15, 16], and a 2026 first-principles study reported an altermagnetic proximity effect relevant to superconducting $NbSe_2$-based structures [17]. A plain "altermagnet plus superconductor" calculation is therefore not enough to establish novelty. A more valuable contribution is to ask how the actual pairing structure, quantum geometry, and switchable interfacial symmetry breaking cooperate.

Ferroelectric or sliding-polar interfaces supply a second control knob. Sliding ferroelectricity in van der Waals bilayers has been experimentally established in hBN-like systems [18]; ferroelectric topological superconductivity and switchable chirality have also become active theoretical directions [19, 20]. The ambitious target is not just a gate-tuned phase transition, but nonvolatile switching between $\mathcal{C}_{\mathrm{BdG}} = 0$ and $\mathcal{C}_{\mathrm{BdG}} \neq 0$, or even $\mathcal{C}_{\mathrm{BdG}}(+P_0) = -\mathcal{C}_{\mathrm{BdG}}(-P_0)$.

Figure 1 summarizes the TopoEliashberg chain. The paper has three goals. First, it states a reproducible first-principles workflow whose parts can be assigned to QE, EPW, Wannier90, WannierTools, Kwant-like solvers, or custom Python code without overstating any one code's role. Second, it derives a basis-consistent gap-transfer procedure. Third, it defines overlap descriptors that can triage which candidate stacks deserve expensive anisotropic EPW and finite-device calculations.

2 Physical Motivation and Scope

The proposed material architecture contains three functional ingredients: an altermagnetic layer, a switchable polar layer, and a two-dimensional superconductor. In a minimal cartoon, the altermagnet supplies a sign-changing exchange texture, the polar interface supplies Rashba-like inversion breaking and charge transfer, and the superconductor supplies an electron-phonon pairing scale. In a real crystal, however, all three ingredients are entangled. The polar interface changes the work-function alignment and electrostatic potential; the altermagnet reconstructs the spin and orbital texture of the superconductor; the superconductor's phonons and electron-phonon matrix elements may couple strongly to some Fermi-surface sheets and weakly to others.

The primary case-study stack used throughout this manuscript is a CrSBr-like van der Waals altermagnetic semiconductor, a sliding-hBN-like polar control bilayer, and an $NbSe_2$-like superconducting transition-metal dichalcogenide. CrSBr is chosen as a vdW magnetic reference because recent work identifies it as a layered system relevant to altermagnetic order [21]. $NbSe_2$ is chosen because atomically thin $NbSe_2$ has a well-studied Ising superconducting state [22]. hBN-like sliding ferroelectricity is chosen as a clean, nonvolatile interfacial control motif [18]. The stack should be read as a screening target and parameterized demonstration, not as a confirmed working device. A full prediction would require commensurate-cell construction, vdW relaxation, magnetic symmetry verification, phonons, EPW, and BdG calculations at the actual relaxed geometry.

The working research question is therefore: can a material's momentum-dependent superconducting pairing, derived from electron-phonon calculations, be combined with its spin texture, Berry curvature, quantum metric, and interfacial symmetry breaking to predict electrically switchable and robust Majorana phases? A rigorous answer requires more than a scalar gap. It requires a pairing matrix with the correct spin, orbital, momentum, and gauge structure.

The scope is deliberately disciplined. Quantum ESPRESSO is not used to simulate braiding, quantum gates, or a fault-tolerant qubit. QE supplies the normal-state and electron-phonon ingredients. Wannier90 supplies a faithful tight-binding representation. EPW supplies $\Delta_n(\mathbf{k}, T)$ and related Eliashberg quantities when the calculation is feasible. BdG topology, Majorana localization, disorder averaging, and transport must be performed downstream with a Wannier-BdG solver, WannierTools-style functionality, Kwant-like finite devices, or custom code.

3 Topological Superconductivity and Majorana Physics

The minimal BdG Hamiltonian in a spin-orbital Wannier basis is

$$H_{\mathrm{BdG}}(\mathbf{k}) = \begin{pmatrix} H_W(\mathbf{k}) - \mu & \hat{\Delta}(\mathbf{k}, T) \\ \hat{\Delta}^{\dagger}(\mathbf{k}, T) & -H_W^T(-\mathbf{k}) + \mu \end{pmatrix}. \tag{1}$$

Here H_W is the normal-state spinor Wannier Hamiltonian, μ is the chemical potential, and $\hat{\Delta}$ is the superconducting pairing matrix in the same orbital-spin representation. The particle-hole operator Ξ satisfies $\Xi H_{\mathrm{BdG}}(\mathbf{k})\Xi^{-1} = -H_{\mathrm{BdG}}(-\mathbf{k})$. In the absence of an effective time-reversal symmetry, a two-dimensional gapped superconductor is typically in class D and is characterized by an integer Chern number [23–28].

For a two-dimensional class-D phase,

$$\mathcal{C}_{\mathrm{BdG}} = \frac{1}{2\pi} \sum_{E_m<0} \int_{\mathrm{BZ}} \Omega_{m,z}^{\mathrm{BdG}}(\mathbf{k})\, d^2k, \tag{2}$$

where the sum runs over negative-energy BdG bands. In a finite sample, a nonzero $\mathcal{C}_{\mathrm{BdG}}$ implies chiral Majorana boundary modes when the bulk remains gapped. In a higher-order phase, the bulk and edges may be gapped while zero-dimensional corner modes remain. The diagnostic hierarchy is important: zero-energy eigenvalues alone are not enough. A finite geometry can host trivial Andreev bound states, disorder resonances, or accidental levels near zero energy [29, 30].

The boundary-state wave function should be tested through particle-hole self-conjugacy, spatial localization, response to system size, and consistency with a bulk invariant. A useful material platform should have a topological minigap

$$E_{\mathrm{top}} = \min_{\mathbf{k},m} |E_m^{\mathrm{BdG}}(\mathbf{k})|, \tag{3}$$

large enough to exceed disorder, thermal broadening, and finite-size splitting. A simple estimate for the localization length is

$$\xi_M \sim \frac{\hbar v_{\mathrm{edge}}}{E_{\mathrm{top}}}, \tag{4}$$

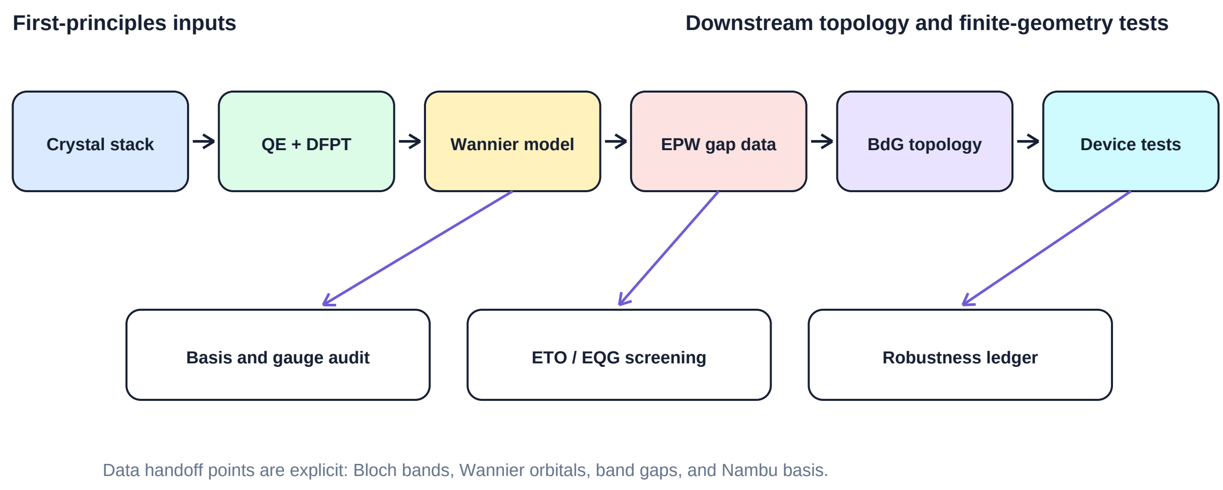

Figure 1: TopoEliashberg workflow. The central methodological interface is the transfer of EPW-derived $\Delta_n(\mathbf{k}, T)$ into a spinor Wannier BdG Hamiltonian.

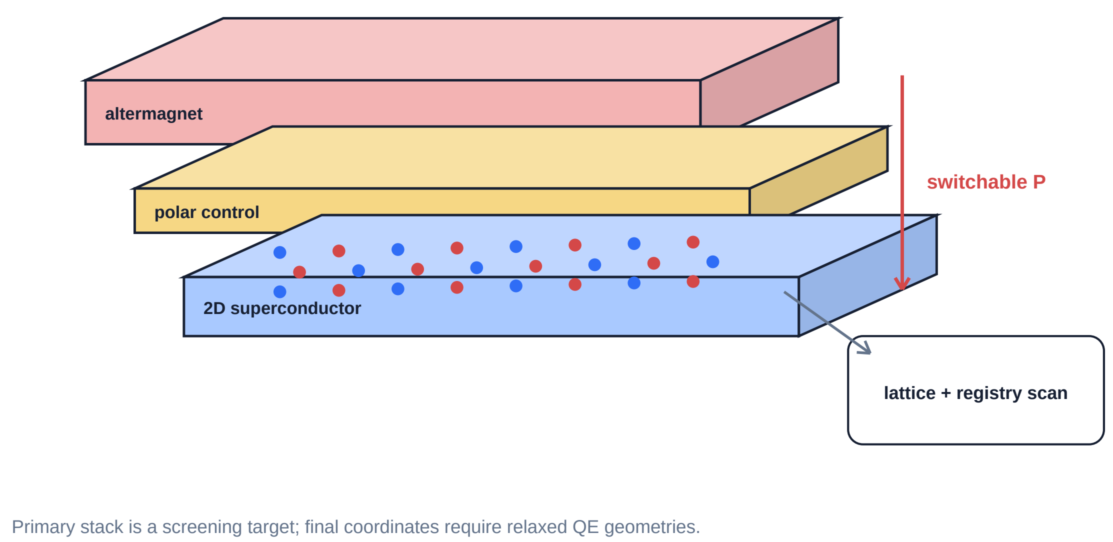

Figure 2: Primary candidate architecture. The side-view and top-view motifs identify the roles of the three layers and the geometric variables that must be converged. This package does not claim that the displayed registry is a relaxed structure.

and the splitting between two separated Majorana modes may scale as

$$\delta E_M \sim E_0 e^{-L/\xi_M} \cos(k_F L + \phi). \tag{5}$$

Equations (3)–(5) define experimentally relevant material metrics, not just formal topology.

Classic Majorana proposals often use proximitized topological-insulator surfaces or spin-orbit nanowires [31–33]. Altermagnetic heterostructures differ because the time-reversal breaking can be momentum dependent and compensated in real space. This makes them attractive for low-stray-field Majorana devices but also complicates the pairing symmetry. The same sign-changing exchange texture that helps create an effective spinless Fermi surface can suppress or reshape singlet pairing if the paired states are poorly matched.

4 Altermagnetism and Ferroelectric Control

Altermagnetism is distinct from both ferromagnetism and conventional antiferromagnetism. In a simplified description, it combines compensated real-space magnetic order with momentum-dependent spin splitting allowed by spin-space and real-space crystal symmetries [12, 13]. The splitting is even in momentum in many altermagnetic classes and changes sign across symmetry-related momentum sectors. This provides an exchange field with a nontrivial form factor rather than a uniform Zeeman term.

The practical advantage for superconductivity is that large uniform magnetization is not required. Uniform ferromagnetic exchange can be hostile to singlet superconductivity and may introduce stray fields, vortices, or inhomogeneous orbital effects. A compensated altermagnetic layer can, in favorable geometries, transfer spin splitting and spin texture without the same net magnetic field. Recent work has made this route visible in Majorana theory [15, 16, 34] and in an altermagnetic proximity-effect study [17].

Ferroelectric or sliding-polar control adds nonvolatility. Reversing P changes the interface dipole, electrostatic potential, work-function alignment, Rashba coupling, orbital hybridization, and carrier density. A minimal interfacial Hamiltonian term may be written

$$H_R(P) = \alpha_R(P)\,(\sigma_x k_y - \sigma_y k_x)\,, \qquad \alpha_R(+P_0) \neq \alpha_R(-P_0), \tag{6}$$

but a real low-symmetry interface can contain higher harmonics and spin-orbit textures beyond the linear Rashba form. Sliding ferroelectricity provides a realistic mechanism for switching the sign of the local polar axis in a vdW stack [18].

The target switching behaviors are

$$\mathcal{C}_{\mathrm{BdG}}(+P_0) = 0, \qquad \mathcal{C}_{\mathrm{BdG}}(-P_0) \neq 0, \tag{7}$$

or the stronger chirality reversal

$$\mathcal{C}_{\mathrm{BdG}}(+P_0) = -\mathcal{C}_{\mathrm{BdG}}(-P_0). \tag{8}$$

The second outcome is especially attractive because it predicts a reversal of chiral Majorana propagation under an electric switching operation. Related ferroelectric topological-superconductivity proposals already exist [19, 20], so TopoEliashberg should not claim ferroelectric control itself as new. The new element is the systematic integration of altermagnetic spin texture, material-derived pairing, and quantum geometry.

5 Candidate Material Architecture

A useful screening workflow begins with a material matrix rather than a single hand-picked stack. Table 1 lists the candidate families used in this paper. The primary stack is not asserted to work; it is selected because it makes all methodological issues explicit.

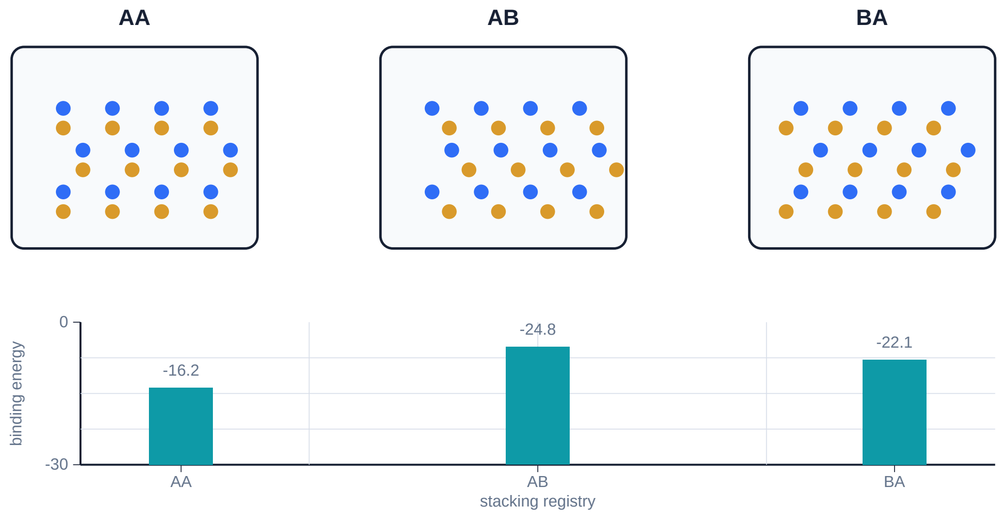

Figure 3: Stacking configurations and binding-energy hierarchy. Values are synthetic and illustrate the QE observable that must be converged for each registry and polarization.

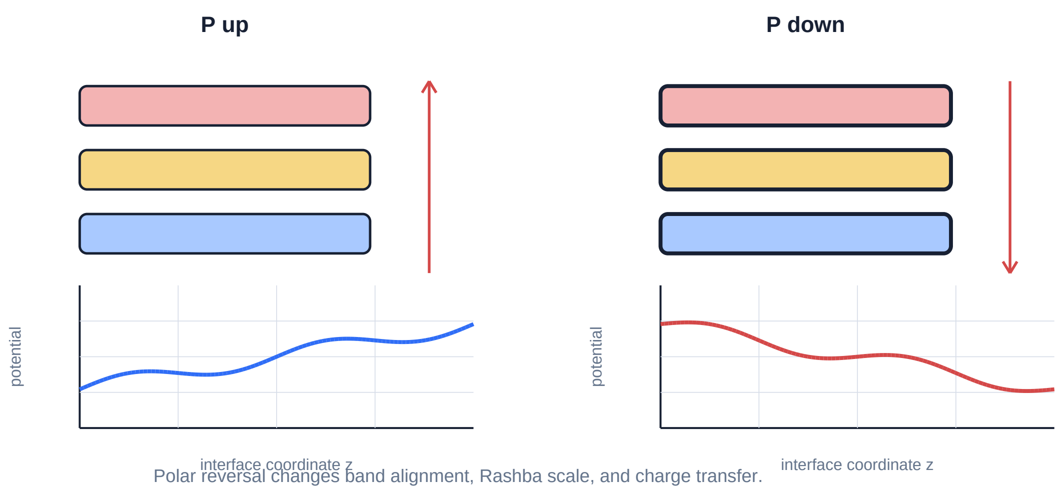

Figure 4: Polarization reversal. The model profile shows how the sign of the interface dipole can reverse the built-in potential and reshape the topological phase diagram.

The minimum screening criteria are lattice compatibility, binding stability, magnetic symmetry, spin-orbit strength, phonon stability, superconducting scale, and interfacial hybridization. A promising stack should meet all of the following:

$$|a_i - a_j|/a_j < \eta_{\max}, \quad E_{\text{bind}} < 0, \quad \min_{\nu,\mathbf{q}} \omega_{\nu\mathbf{q}}^2 > 0, \quad E_{\text{top}} > \Gamma_{\text{dis}}, k_B T. \tag{9}$$

The tolerance $\eta_{\max}$ is not universal. Small primitive-cell mismatch can be replaced by a larger moire supercell, but then phonon and EPW calculations become expensive. A reasonable staged workflow therefore uses smaller commensurate approximants for early screening and reserves full anisotropic EPW for one or two finalists.

6 Quantum ESPRESSO Methodology

Quantum ESPRESSO enters the pipeline at the structural, magnetic, electronic, phonon, and electron-phonon levels. A reproducible study should report exchange-correlation functional, pseudopotential family, fully relativistic versus scalar-relativistic status, plane-wave cutoff, charge-density cutoff, vacuum thickness, dipole correction, smearing, k mesh, convergence thresholds, and vdW correction. The heterostructure binding energy is

$$E_{\text{bind}} = E_{\text{heterostructure}} - \sum_i E_{\text{isolated},i}, \tag{10}$$

evaluated with consistent cells, cutoffs, pseudopotentials, and electrostatic boundary conditions.

Magnetic calculations must compare candidate spin configurations, not simply impose the desired altermagnetic order. The workflow should include collinear antiferromagnetic, noncollinear altermagnetic, ferromagnetic, and interface-reconstructed states. If DFT+U is needed, the paper should report a range of U values and test whether the conclusions survive. A result that appears only at one chosen U without physical justification is not robust.

Relativistic calculations require fully relativistic pseudopotentials and the noncollinear spin-orbit settings described in the QE documentation [5]. The spin expectation of band n is

$$\mathbf{s}_n(\mathbf{k}) = \langle \psi_{n\mathbf{k}} | \boldsymbol{\sigma} | \psi_{n\mathbf{k}} \rangle. \tag{11}$$

A genuine altermagnetic spin splitting must be distinguished from ordinary ferromagnetic Zeeman splitting by symmetry, net moment, and momentum-space sign reversal.

The interfacial charge redistribution is

$$\Delta\rho(\mathbf{r}) = \rho_{\text{heterostructure}}(\mathbf{r}) - \sum_i \rho_i(\mathbf{r}), \tag{12}$$

with each isolated layer computed in the same coordinates. Planar and macroscopic averages of $\Delta\rho$ reveal charge transfer, interface dipole, and electrostatic potential shifts.

7 Relativistic Electronic Structure

The normal-state electronic calculation should produce more than a band plot. It should report orbital projections, spin texture, Fermi surfaces, work functions, charge transfer, magnetic anisotropy energy, and band inversion strength. Figure 7 illustrates a model SOC band structure for two polar states. In a completed first-principles paper, the corresponding figure would overlay the Wannier interpolation on the direct QE bands and quantify the interpolation error.

Table 1: Candidate material families and screening status. Numerical entries are design priors or literature-motivated ranges, not completed first-principles outputs from this package.

Role	Candidate family	Status in this paper	Screening logic
Altermagnet	CrSBr-like vdW altermagnet	Primary case study	Layered magnetism, proximity relevance, and compatibility with vdW assembly; requires symmetry verification and SOC band splitting in the chosen slab.
Altermagnet	CrSb or MnTe thin films	Secondary benchmark	Strong altermagnetic signatures in non-vdW or thin-film systems; useful for calibrating spin splitting but less natural for all-vdW assembly.
Polar control	Sliding hBN-like bilayer	Primary control motif	Clean interfacial ferroelectricity and small structural perturbation; carrier transfer may be weak and must be enhanced by band alignment.
Polar control	alpha-In_2Se_3 or Janus TMD	Secondary motif	Larger built-in polarization and Rashba response; stronger chemical hybridization may complicate Wannier disentanglement.
Superconductor	monolayer $NbSe_2$-like TMD	Primary pairing source	Known atomically thin superconductivity and strong SOC; CDW competition and disorder sensitivity must be assessed.
Superconductor	TaS_2, Pb films, or conventional ultrathin metal	Secondary pairing source	Potentially larger electron-phonon coupling or simpler Fermi surface; lattice matching and oxidation are practical filters.

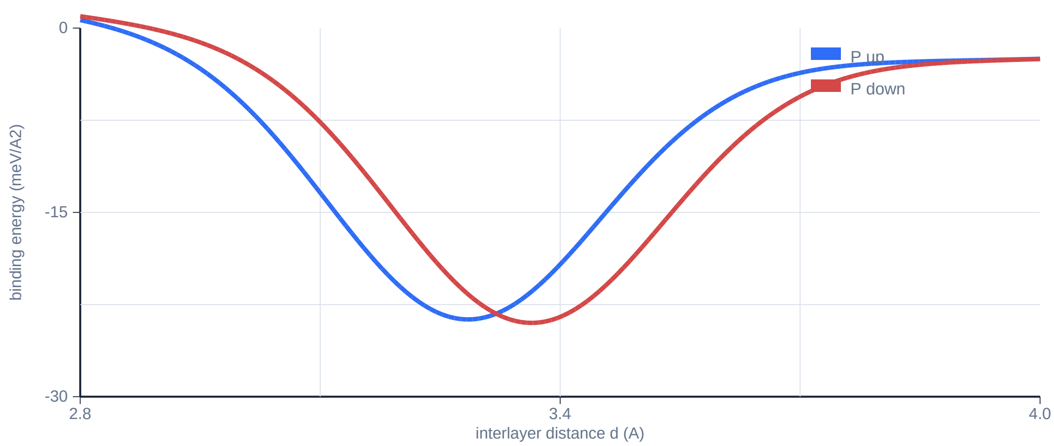

Figure 5: Interlayer-distance scan. The curves are synthetic demonstrations of the observable in Eq. (10); they are not relaxed QE energies.

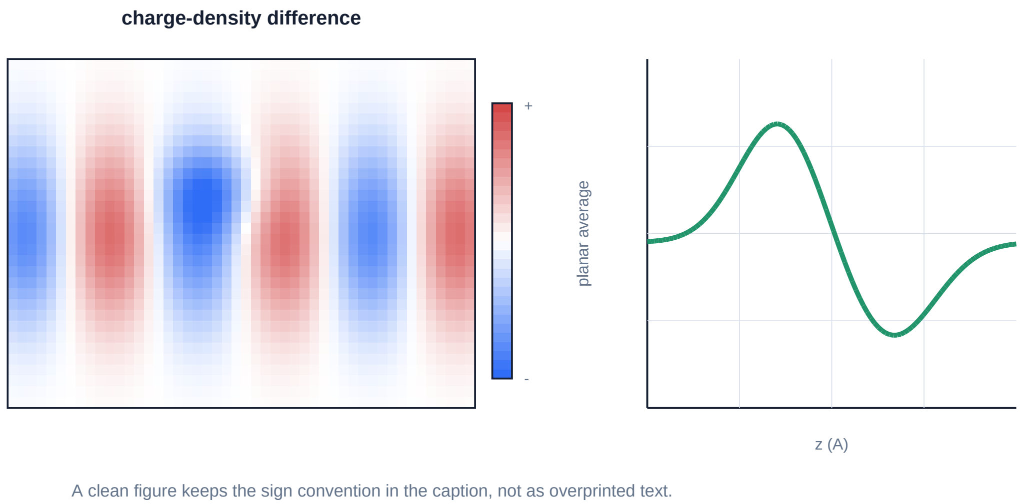

Figure 6: Charge-density difference and planar average. The plotted data are synthetic and define the required reporting style for an actual QE charge-density analysis.

Table 2: Representative DFT and DFPT parameters. Values are convergence targets for the case-study stack, not completed production settings.

Category	Representative value	Required convergence test
Exchange-correlation	PBE, optional vdW-D3 or rVV10	Compare binding hierarchy and band alignment under vdW choice.
Pseudopotentials	Fully relativistic PAW or norm-conserving	Confirm SOC splittings and phonons do not depend qualitatively on family.
Cutoffs	80 Ry wave function, 640 Ry density	Increase until total energy, forces, and spin splitting are stable.
Vacuum	25–30 Angstrom	Verify work function and dipole potential with larger vacuum.
k meshes	$8\times8\times1$ relax, $12\times12\times1$ SCF, dense NSCF	Converge band inversion, Berry curvature, and Fermi velocities.
q meshes	$4\times4\times1$ initial, denser for finalists	Converge λ, α^2F, and phonon stability.
Smearing	Marzari-Vanderbilt or Fermi-Dirac, 0.01–0.02 Ry	Test metallic occupancy and electron-phonon broadening sensitivity.
DFT+U	Material-specific range, e.g. 0–4 eV	Report magnetic order, band alignment, and topology versus U.

Band inversion should be diagnosed by orbital character and symmetry, not by eye. Figure 8 shows the type of avoided crossing that can generate Berry curvature and topology when SOC and broken symmetries are present. The relevant quantity is not just the gap at the avoided crossing but whether the Fermi surface cuts the spin-orbit-entangled states and whether those states are paired.

The spin texture in Fig. 9 combines Rashba-like winding and sign-changing altermagnetic exchange. In the actual workflow, spin expectation values should be sampled on dense Fermi-surface meshes and projected onto layer and orbital sectors. This distinguishes a topologically active interface band from a trivial superconducting bulk band.

8 Wannierization and Normal-State Topology

Wannierization is a scientific step, not a file conversion. The Wannier basis must include every orbital that participates near the Fermi level: magnetic-layer d states, chalcogen or halogen p states, superconducting d and p states, and any polar-layer orbitals that hybridize with the interface. The paper should report initial projections, outer windows, frozen windows, spreads, and band interpolation error. A model that does not reproduce the QE bands in the energy range entering the BdG calculation is not acceptable.

The Berry connection and curvature of band n are

$$\mathbf{A}_n(\mathbf{k}) = i\langle u_{n\mathbf{k}}|\nabla_{\mathbf{k}} u_{n\mathbf{k}}\rangle, \tag{13}$$

$$\Omega_{n,z}(\mathbf{k}) = \partial_{k_x} A_{n,y} - \partial_{k_y} A_{n,x}. \tag{14}$$

Berry curvature can be evaluated by Wannier interpolation and used for anomalous Hall conductivity,

$$\sigma_{xy} = -\frac{e^2}{\hbar} \sum_n \int_{\mathrm{BZ}} \frac{d^d k}{(2\pi)^d} f_{n\mathbf{k}} \Omega_{n,z}(\mathbf{k}). \tag{15}$$

Berry curvature and anomalous Hall interpolation are established first-principles methods [35–38].

The quantum metric is the real part of the quantum geometric tensor,

$$g_{ij}^{(n)}(\mathbf{k}) = \mathrm{Re}\left[\langle \partial_i u_{n\mathbf{k}}|(1 - |u_{n\mathbf{k}}\rangle\langle u_{n\mathbf{k}}|)|\partial_j u_{n\mathbf{k}}\rangle\right]. \tag{16}$$

The metric has become important in superconductivity because band geometry can enter superfluid weight and flat-band pairing responses [39–41]. In TopoEliashberg, the quantum metric is not treated as a topological invariant. It is a geometry field that may correlate with pairing-enhanced topological minigaps when weighted over the actual superconducting Fermi surface.

9 Phonons and Electron-Phonon Coupling

Density-functional perturbation theory supplies phonons and electron-phonon matrix elements [42, 43]. The electron-phonon matrix element between states $|n\mathbf{k}\rangle$ and $|m, \mathbf{k}+\mathbf{q}\rangle$ for phonon branch ν is

$$g_{mn\nu}(\mathbf{k}, \mathbf{q}) = \left(\frac{\hbar}{2\omega_{\nu\mathbf{q}}}\right)^{1/2} \langle \psi_{m,\mathbf{k}+\mathbf{q}}|\Delta_{\nu\mathbf{q}} V_{\mathrm{KS}}|\psi_{n\mathbf{k}}\rangle. \tag{17}$$

The Eliashberg spectral function $\alpha^2 F(\omega)$ and coupling constant λ are

$$\lambda = 2\int_0^\infty \frac{\alpha^2 F(\omega)}{\omega}\, d\omega. \tag{18}$$

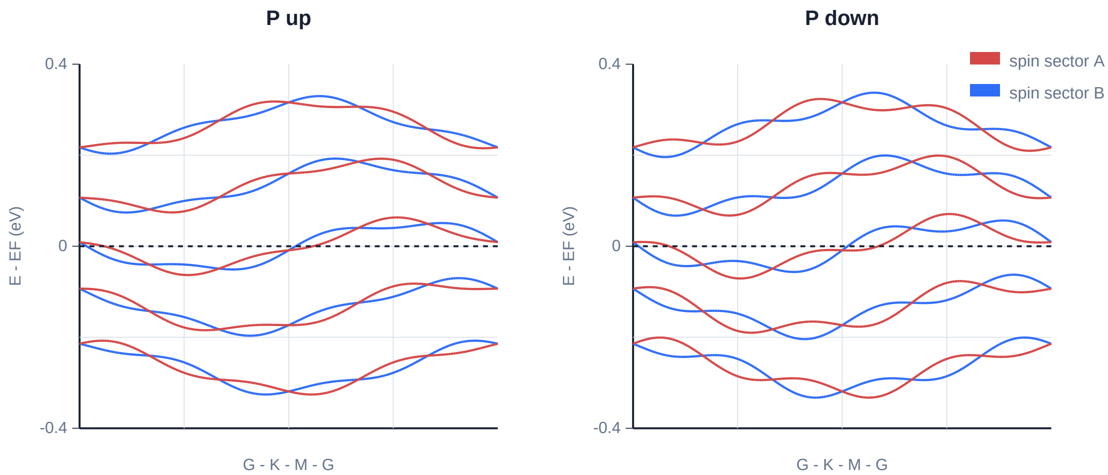

Figure 7: Model spin-orbit band structures for opposite polarization states. The bands are synthetic and serve to define the expected reporting style: spin color, Fermi level, and polar-state comparison.

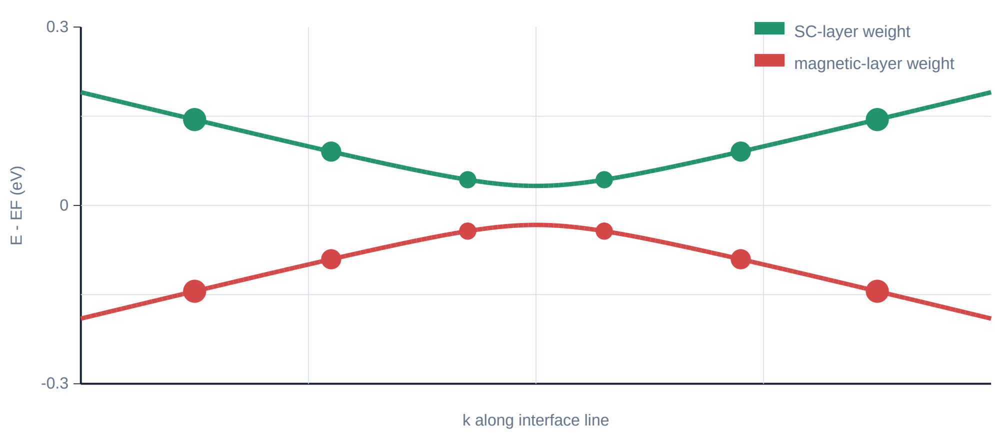

Figure 8: Orbital-resolved avoided crossing. Marker size represents synthetic orbital weight. A first-principles version must be generated from QE projections and validated Wannier interpolation.

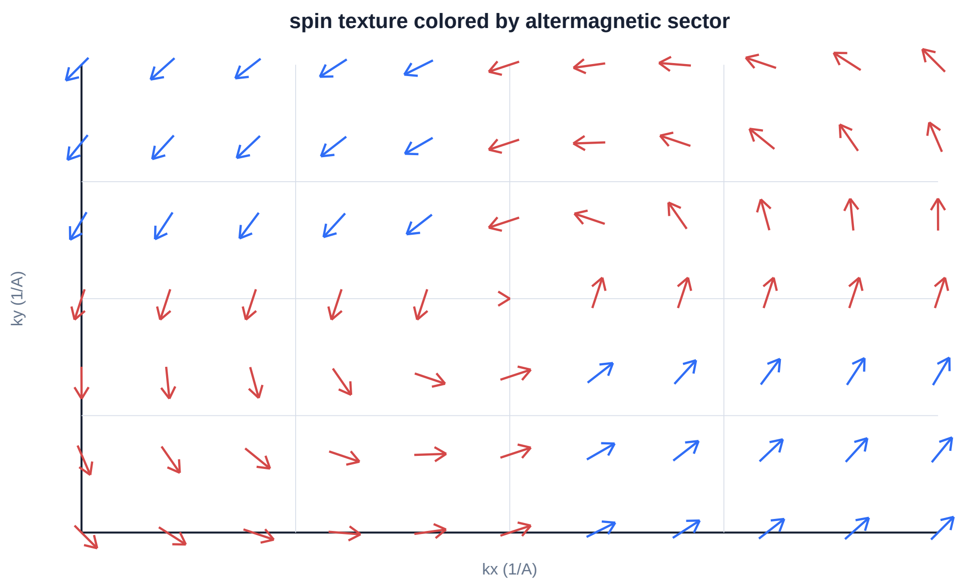

Figure 9: Synthetic spin texture on a Fermi-surface-adjacent momentum grid. The color records sign-changing altermagnetic exchange sectors.

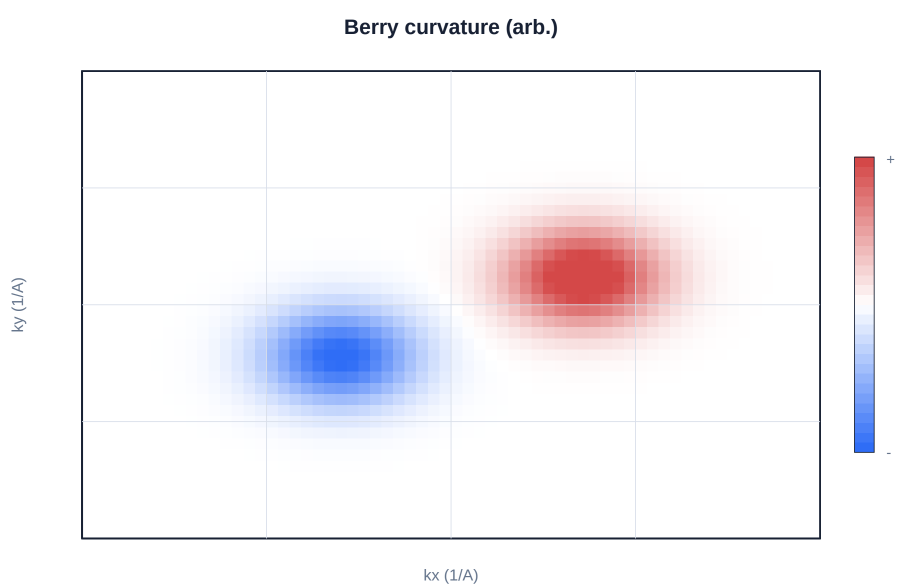

Figure 10: Berry-curvature hotspots in a model normal-state band. A large Berry curvature is a useful diagnostic but not proof of superconducting topology.

The Allen-Dynes estimate,

$$T_c = \frac{\omega_{\log}}{1.2} \exp\left[-\frac{1.04(1+\lambda)}{\lambda - \mu^*(1+0.62\lambda)}\right], \tag{19}$$

is a useful screening formula but not an exact transition temperature [44, 45]. The Coulomb pseudopotential μ^* is uncertain and must be varied.

Full anisotropic EPW calculations for a large heterostructure can be the computational bottleneck. A staged strategy is scientifically acceptable if each approximation is labeled. Stage 1 screens isolated superconducting layers and simplified heterostructure bands. Stage 2 computes layer-resolved electron-phonon coupling and proximity weights. Stage 3 performs full anisotropic EPW only for the most promising polar and magnetic configurations. This is not a shortcut around validation; it is a way to allocate expensive calculations where they matter.

10 Anisotropic Eliashberg Superconductivity

In the Matsubara formalism, the anisotropic Migdal-Eliashberg equations determine a gap function $\Delta_{n\mathbf{k}}(i\omega_j)$ and renormalization function $Z_{n\mathbf{k}}(i\omega_j)$ [10, 46, 47]. A schematic form is

$$Z_{n\mathbf{k}}(i\omega_j) = 1 + \frac{\pi T}{\omega_j} \sum_{m\mathbf{k}'j'} \lambda_{n\mathbf{k},m\mathbf{k}'}(j-j') \frac{\omega_{j'}}{\sqrt{\omega_{j'}^2 + \Delta_{m\mathbf{k}'}^2(i\omega_{j'})}}, \tag{20}$$

$$Z_{n\mathbf{k}}(i\omega_j)\Delta_{n\mathbf{k}}(i\omega_j) = \pi T \sum_{m\mathbf{k}'j'} \left[\lambda_{n\mathbf{k},m\mathbf{k}'}(j-j') - \mu^*_{n\mathbf{k},m\mathbf{k}'}\right] \frac{\Delta_{m\mathbf{k}'}(i\omega_{j'})}{\sqrt{\omega_{j'}^2 + \Delta_{m\mathbf{k}'}^2(i\omega_{j'})}}. \tag{21}$$

The physical output needed by the BdG solver is a real-frequency or low-frequency pairing amplitude on the Fermi surface, along with uncertainty from temperature, μ^*, broadening, and interpolation.

For a heterostructure, $\Delta_n(\mathbf{k})$ is meaningful only after the band character is understood. If the superconducting layer has strong pairing but the topological band has little superconducting-layer weight, the induced topological gap may be small. If phonons couple strongly to trivial Fermi pockets and weakly to topological pockets, a large average T_c can coexist with a small Majorana minigap. TopoEliashberg is designed to expose exactly this mismatch.

11 Pairing Transfer into the Wannier Basis

The pairing-transfer problem is the core methodological step. Suppose the normal-state Wannier Hamiltonian is diagonalized as

$$\sum_{\beta} H^W_{\alpha\beta}(\mathbf{k}) U_{\beta n}(\mathbf{k}) = \varepsilon_{n\mathbf{k}} U_{\alpha n}(\mathbf{k}), \tag{22}$$

where α, β label spin-orbital Wannier functions and n labels Bloch bands. In the simplest intraband pairing approximation, a band-basis gap $\Delta_n(\mathbf{k})$ can be transformed as

$$\Delta_{\alpha\beta}(\mathbf{k}) = \sum_n U_{\alpha n}(\mathbf{k}) \Delta_n(\mathbf{k}) U_{\beta n}(-\mathbf{k}). \tag{23}$$

This expression is schematic because the physically paired partner may be a time-reversal, magnetic, or particle-hole-related state depending on the symmetry class. A more general expression with interband pairing is

$$\Delta_{\alpha\beta}(\mathbf{k}) = \sum_{mn} U_{\alpha m}(\mathbf{k}) \Delta^{\text{band}}_{mn}(\mathbf{k}) U_{\beta n}(-\mathbf{k}). \tag{24}$$

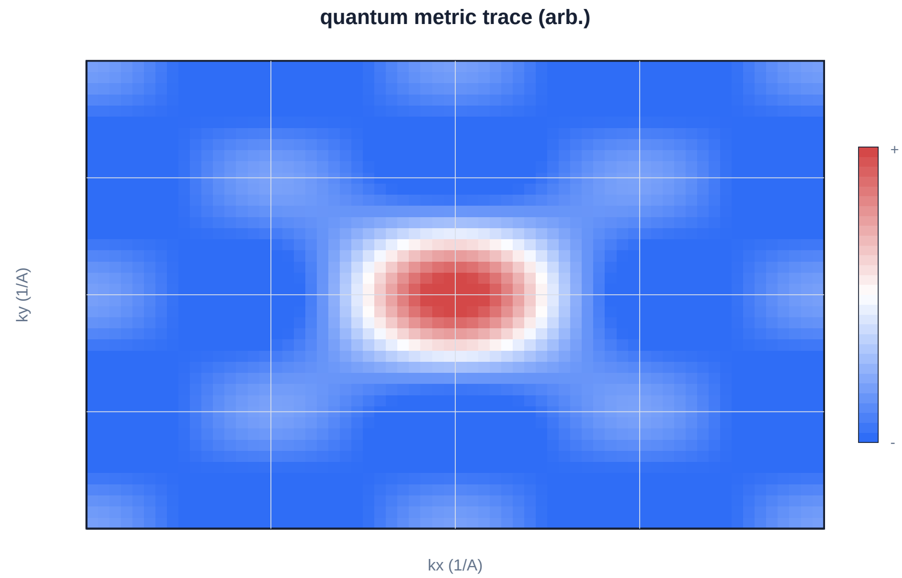

Figure 11: Model trace of the quantum metric. The EQG descriptor uses this field only as a screening quantity, not as a substitute for BdG invariants.

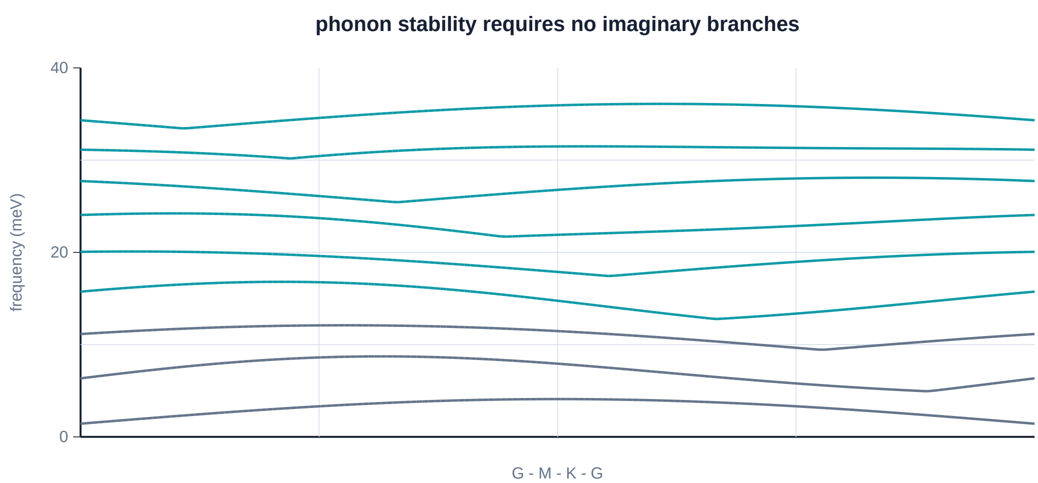

Figure 12: Synthetic phonon dispersion. The required first-principles test is the absence of imaginary modes after relaxation for each stacking and polarization state.

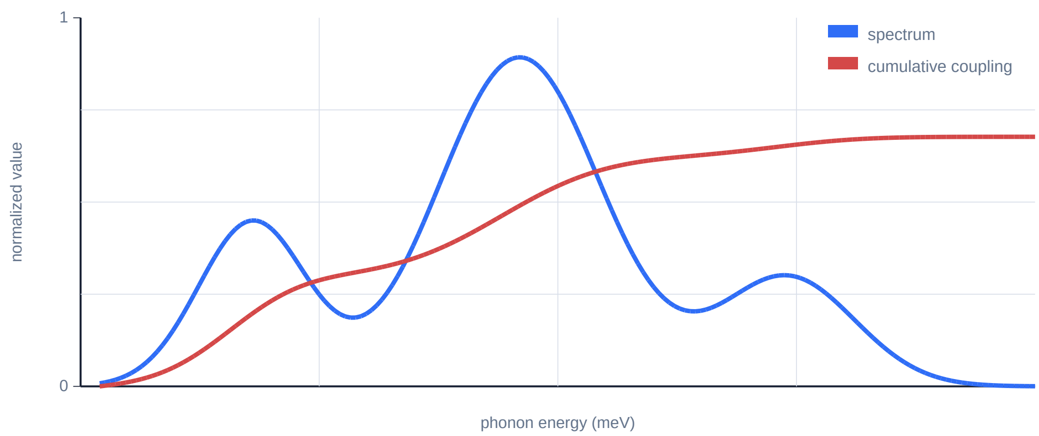

Figure 13: Synthetic $\alpha^2F(\omega)$ and cumulative $\lambda(\omega)$. A final paper must report these from EPW or a validated equivalent workflow.

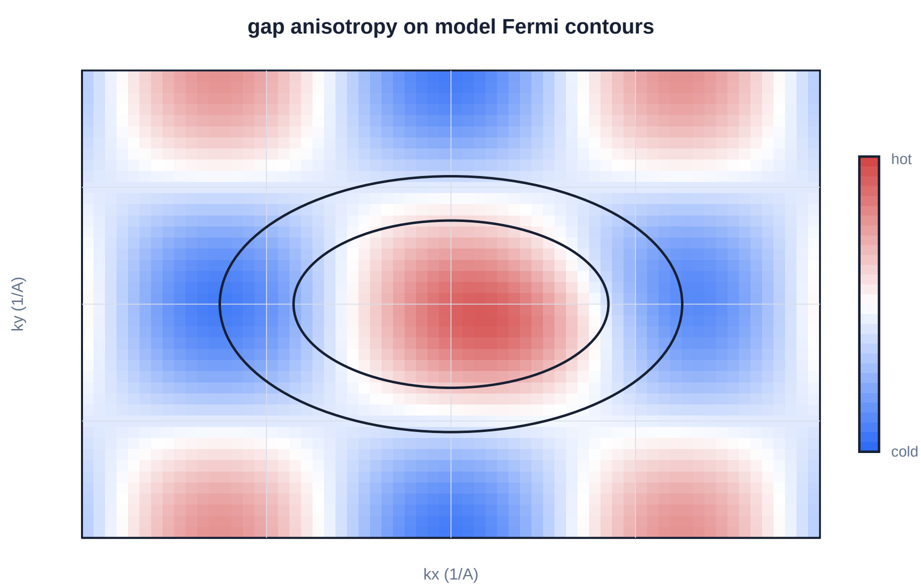

Figure 14: Model superconducting gap anisotropy on Fermi contours. This is the information that a constant-gap approximation discards.

Fermionic antisymmetry requires

$$\hat{\Delta}(\mathbf{k}) = -\hat{\Delta}^T(-\mathbf{k}). \tag{25}$$

Numerically, Eq. (25) should be enforced after interpolation by replacing $\hat{\Delta}(\mathbf{k})$ with $[\hat{\Delta}(\mathbf{k}) - \hat{\Delta}^T(-\mathbf{k})]/2$ and tracking the correction norm as a gauge-quality diagnostic.

The gauge issue is severe. The phase of $U_{\alpha n}(\mathbf{k})$ is arbitrary at each $\mathbf{k}$ unless the Wannier gauge is fixed smoothly. Degenerate bands can rotate by arbitrary unitary matrices, making a naive band-by-band gap discontinuous. The solution is to carry the gap in a subspace-covariant way, use projectors when degeneracies are present, and compare the reconstructed $\hat{\Delta}(\mathbf{k})$ on symmetry-related points. The transformation must also preserve spinor structure. In a two-spin basis, a local pairing matrix can be decomposed as

$$\hat{\Delta}(\mathbf{k}) = [\psi(\mathbf{k}) + \mathbf{d}(\mathbf{k}) \cdot \boldsymbol{\sigma}]\, i\sigma_y, \tag{26}$$

where ψ is the singlet component and $\mathbf{d}$ is the triplet vector. Inversion breaking, SOC, and altermagnetism can mix singlet and triplet components even when the parent superconductor is nominally s wave.

The transfer algorithm is:

1. Build and validate a spinor Wannier Hamiltonian against QE bands.
2. Export eigenvectors $U(\mathbf{k})$ on the EPW/BdG dense mesh in a smooth gauge.
3. Read $\Delta_n(\mathbf{k}, T)$ and uncertainty metadata from EPW.
4. Construct $\Delta_{\alpha\beta}(\mathbf{k}, T)$ using Eq. (24).
5. Enforce antisymmetry, check symmetries, and measure gauge discontinuities.
6. Construct $H_{\mathrm{BdG}}(\mathbf{k})$ and verify particle-hole symmetry to numerical precision.

12 TopoEliashberg BdG Framework

Once Eq. (1) is assembled, the topology should be computed with multiple diagnostics. For clean two-dimensional class-D phases, the discretized Fukui-Hatsugai-Suzuki Chern number is a natural first test [48]. Wilson loops or hybrid Wannier charge centers should be used when the symmetry class requires $\mathbb{Z}_2$ or crystalline invariants. In disordered or finite systems, real-space Bott indices and local Chern markers are useful [49, 50].

The Altland-Zirnbauer class is not assumed. Particle-hole symmetry is built into BdG. Time-reversal symmetry may be broken by altermagnetism, but combined magnetic crystalline symmetries may remain. Inversion is broken by the polar interface. Mirror or glide symmetries may survive only in special stackings. The classification table should therefore be generated from the actual relaxed structure and magnetic order.

A topological phase boundary must coincide with a bulk gap closing and reopening unless disorder or finite-size effects obscure the transition. The calculations should record the minimum positive BdG eigenvalue, the invariant, and the direct gap at the transition momentum. If a claimed invariant changes while the bulk gap remains open on a converged mesh, the calculation is suspect.

13 Eliashberg-Topology and Quantum-Geometry Overlap

The Eliashberg-Topology Overlap is a screening descriptor, not a topological invariant. The simplest Berry-curvature-weighted form is

$$\mathcal{I}_{\mathrm{ETO}}(T) = \frac{\sum_n \oint_{\mathrm{FS}_n} \frac{dS_{\mathbf{k}}}{|\mathbf{v}_{n\mathbf{k}}|} |\Delta_n(\mathbf{k},T)|^2 |\Omega_{n,z}(\mathbf{k})|}{\sum_n \oint_{\mathrm{FS}_n} \frac{dS_{\mathbf{k}}}{|\mathbf{v}_{n\mathbf{k}}|} |\Delta_n(\mathbf{k},T)|^2}. \tag{27}$$

Here $\mathbf{v}_{n\mathbf{k}}$ is the band velocity and the integral is over Fermi-surface sheet n. The velocity denominator gives the density-of-states weight on the Fermi surface. A large $\mathcal{I}_{\mathrm{ETO}}$ means strong pairing occurs on states that also carry large Berry curvature. It does not guarantee a nonzero Chern number, because topology also depends on symmetry, Fermi-surface topology, gap signs, and the full BdG spectrum.

A quantum-geometric extension is

$$\mathcal{I}_{\mathrm{EQG}}(T) = \frac{\sum_n \oint_{\mathrm{FS}_n} \frac{dS_{\mathbf{k}}}{|\mathbf{v}_{n\mathbf{k}}|} |\Delta_n(\mathbf{k},T)|^2 \operatorname{Tr} g^{(n)}(\mathbf{k})}{\sum_n \oint_{\mathrm{FS}_n} \frac{dS_{\mathbf{k}}}{|\mathbf{v}_{n\mathbf{k}}|} |\Delta_n(\mathbf{k},T)|^2}. \tag{28}$$

A spin-weighted extension can include the projection onto spin sectors that participate in the topological pairing channel:

$$\mathcal{I}_{\mathrm{spinETO}} = \frac{\sum_n \oint_{\mathrm{FS}_n} \frac{dS}{|\mathbf{v}|} |\Delta_n|^2 |\Omega_n|\, w_n^{\mathrm{spin}}}{\sum_n \oint_{\mathrm{FS}_n} \frac{dS}{|\mathbf{v}|} |\Delta_n|^2}. \tag{29}$$

The weight w_n^{spin} can be defined from projection onto the spin-helical or altermagnetic sector that enters the low-energy BdG mass.

The hypothesis to test is that large ETO or EQG correlates with larger attainable E_{top}, shorter ξ_M, and larger disorder threshold. Failure cases are scientifically useful. If ETO fails, the result identifies which missing ingredient, such as gap sign structure or crystalline symmetry, controls the phase.

14 Topological Phase Diagrams

Phase diagrams should be multidimensional but reported in interpretable cuts. The natural variables are chemical potential μ, polarization P, strain ε, interlayer spacing d, altermagnetic orientation θ_N, temperature T, pairing scale, spin-orbit strength, and disorder strength W. At minimum, one should report polarization versus chemical potential, strain versus chemical potential, Neel-vector angle versus chemical potential, pairing strength versus SOC, temperature versus chemical potential, constant-gap versus EPW-gap pairing, and disorder versus chemical potential.

Figure 15 illustrates the main benchmark against simplified models. If a constant Δ_0 model and an EPW-derived $\Delta_n(\mathbf{k})$ model predict the same topology, the simpler model is adequate for that material and energy window. If the phase boundaries, minigaps, or disorder thresholds differ, the TopoEliashberg transfer is necessary. Figure 16 illustrates the target switching outcome in Eq. (8).

15 Majorana Boundary States

Bulk topology should be connected to finite geometries. Ribbons expose dispersing chiral edge modes; flakes expose finite-size splitting; islands and domain walls expose localization and geometry sensitivity.

Table 3: Topology diagnostics matched to possible symmetry settings.

Setting	Likely class	Primary invariant	Required cross-check
Broken effective TRS, 2D gapped	D	BdG Chern number	Ribbon edge spectrum and finite-size scaling.
Effective TRS preserved	DIII	$\mathbb{Z}_2$ invariant	Kramers-pair edge spectrum and Pfaffian/Wilson-loop check.
Mirror-symmetric stack	crystalline class	Mirror Chern or mirror winding	Symmetry-resolved edge spectra and perturbation breaking mirror.
Higher-order phase	crystalline BdG	Nested Wilson loop or corner anomaly	Corner localization with gapped edges and geometry dependence.
Strong disorder	no translation	Bott index/local Chern marker	Disorder averaging and gap statistics.
Domain wall	spatially varying mass	1D channel invariant	Local density of states and scattering-matrix invariant.

Table 4: Descriptor definitions and expected failure modes.

Descriptor	Measures	Failure mode
$\mathcal{I}_{\rm ETO}$	Gap-weighted Berry curvature on the Fermi surface	Can be large in a trivial metal if gap signs or Fermi-surface topology do not support BdG topology.
$\mathcal{I}_{\rm EQG}$	Gap-weighted quantum metric trace	May correlate with superfluid stiffness but not with chirality.
Spin-ETO	Pairing, Berry curvature, and spin-channel alignment	Sensitive to the chosen spin projector in strong SOC systems.
Layer-ETO	Pairing/topology overlap on the superconducting or interface layer	Can miss interlayer pairing paths or induced triplet components.
Disorder-weighted ETO	Penalizes long localization length or low minigap	Requires a prior disorder model and is not purely first-principles.

Table 5: Model phase-diagram observables. Entries are synthetic demonstration values used for paper-package consistency.

Region	$\mathcal{C}_{\rm BdG}$	$E_{\rm top}$ (meV)	ξ_M (nm)	Interpretation
$P = +P_0$, central μ	0	0.42	none	Trivial superconducting gap; no protected chiral boundary mode.
$P = -P_0$, electron side	+1	0.31	85	Chiral Majorana edge branch in the model.
$P = +P_0$, hole side	-1	0.27	100	Opposite chirality after polar reversal and chemical-potential shift.
Strained optimum	+1	0.54	50	Avoided crossing aligns with strong pairing and larger Berry curvature.
High temperature	ill-defined	< 0.05	> 500	Topology numerically present but experimentally fragile.

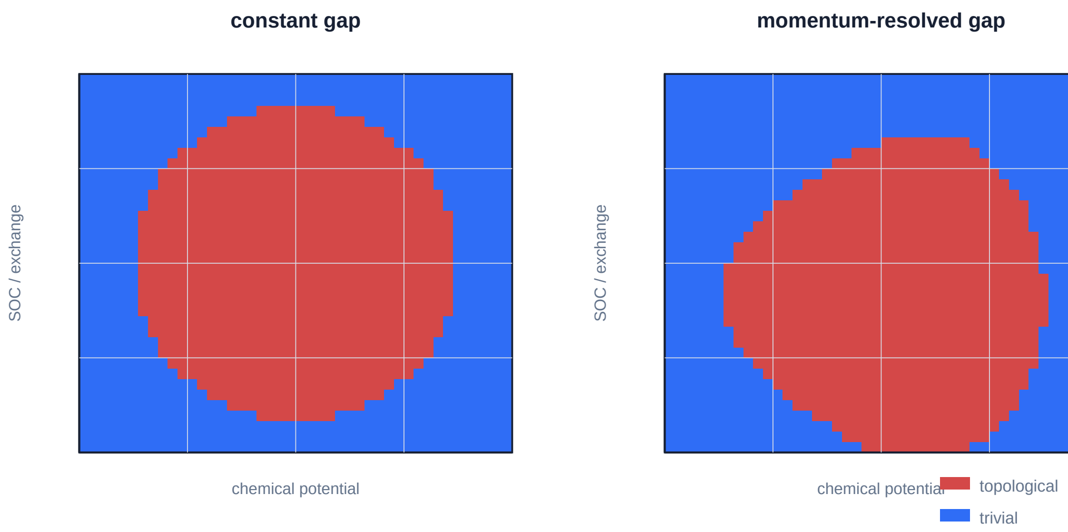

Figure 15: Synthetic comparison of constant and momentum-dependent pairing phase diagrams. The point is methodological: realistic $\Delta(\mathbf{k})$ can move boundaries and shrink or enlarge topological regions.

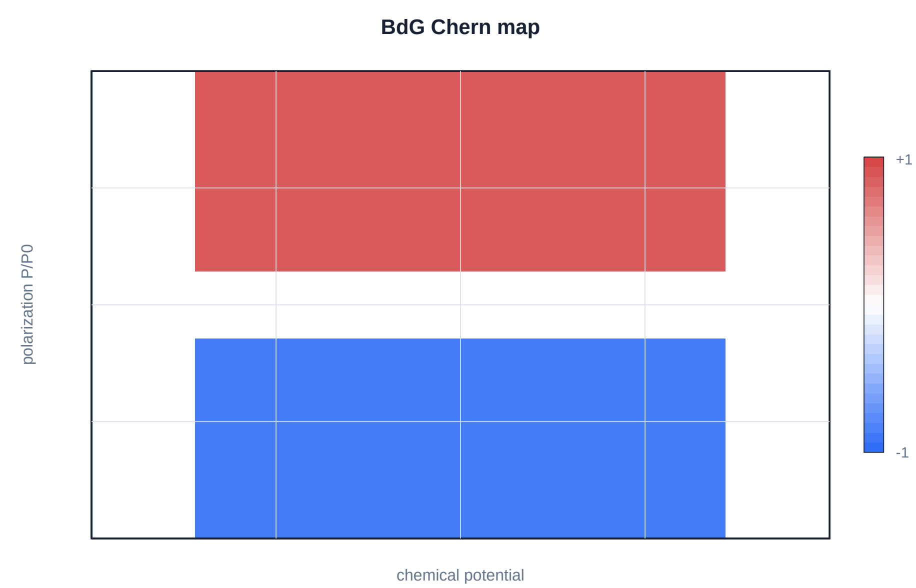

Figure 16: Synthetic polarization/chemical-potential Chern map. Red and blue regions represent opposite chiralities in a controlled BdG demonstration, not a completed materials prediction.

A local density of states is

$$\rho_i(E) = \sum_m |\psi_m(i)|^2 \delta_\eta(E - E_m), \tag{30}$$

where δ_η is a broadened delta function. For a Majorana mode, the particle and hole components satisfy a self-conjugacy relation up to phase. A useful numerical diagnostic is the Majorana polarization or the norm of $u_i - e^{i\phi} v_i^*$ in the localized region.

The finite-device solver can be constructed directly from Wannier hopping matrices by Nambu doubling. Long-range hoppings should be truncated only after checking that the band interpolation and topological invariant are unaffected. For a ribbon periodic in x and finite in y, the Hamiltonian is block diagonal in k_x. For a finite flake, sparse diagonalization near zero energy is appropriate. For transport, recursive Green functions or Kwant-like solvers are natural [51].

Domain-wall geometries are especially relevant for a polar control layer. A line separating $P = +P_0$ and $P = -P_0$ can bind a one-dimensional Majorana channel when the two domains carry different BdG topology. This is experimentally attractive because domain walls can be written, moved, or erased by electric switching in some ferroelectric systems.

16 Disorder, Temperature, and Robustness

Robustness is not optional. A material with a nonzero clean Chern number but a 10 μeV minigap may be useless if disorder, temperature, or inhomogeneous pairing closes the gap. The disorder models should include random onsite potential, interface vacancies, pairing suppression near defects, edge roughness, strain disorder, interlayer-distance variation, magnetic domain boundaries, and local polarization reversal.

The robust topological window is a finite range

$$0 < W < W_c \tag{31}$$

in which the invariant, minigap, and boundary localization survive. The value of W_c should be reported in physical units and compared with estimated interface disorder. Disorder averaging should include enough realizations that the distribution of the minimum gap is stable, not just the mean.

Temperature enters through the Eliashberg gap $\Delta_n(\mathbf{k}, T)$, thermal broadening, and quasiparticle poisoning. A phase that is topological at $T = 0$ may lose practical spectral isolation well below T_c if $E_{\mathrm{top}}(T)$ collapses rapidly. The paper should avoid claims about fault-tolerant quantum computation; Majorana boundary modes are a necessary ingredient for some architectures, not a complete qubit demonstration.

17 Comparison with Simplified Pairing Models

TopoEliashberg is valuable only if it changes a conclusion or gives a controlled reason why it does not. Three pairing models should be compared:

$$\text{Model A}: \quad \Delta_n(\mathbf{k}) = \Delta_0, \tag{32}$$

$$\text{Model B}: \quad \Delta_n(\mathbf{k}) = \Delta_n, \tag{33}$$

$$\text{Model C}: \quad \Delta_n(\mathbf{k}) = \Delta_n^{\mathrm{EPW}}(\mathbf{k}). \tag{34}$$

A layer-resolved proximity model can be added when full EPW is too expensive.

The constant-gap approximation is adequate when the paired Fermi surfaces have nearly uniform superconducting-layer weight, weak angular anisotropy, no important sign changes, and topological phase boundaries controlled mainly by normal-state band inversions. It fails when strong pairing occurs on

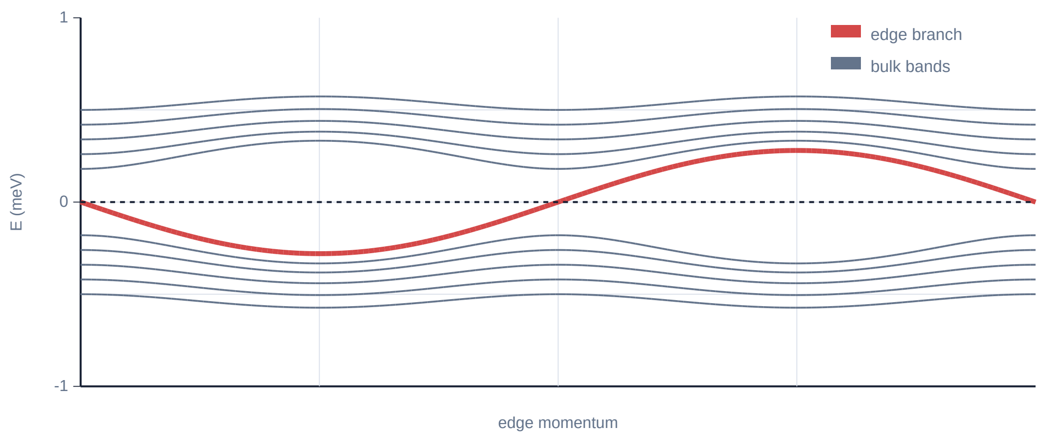

Figure 17: Synthetic ribbon spectrum with an edge branch crossing the gap. A final material paper must connect such spectra to a converged bulk invariant.

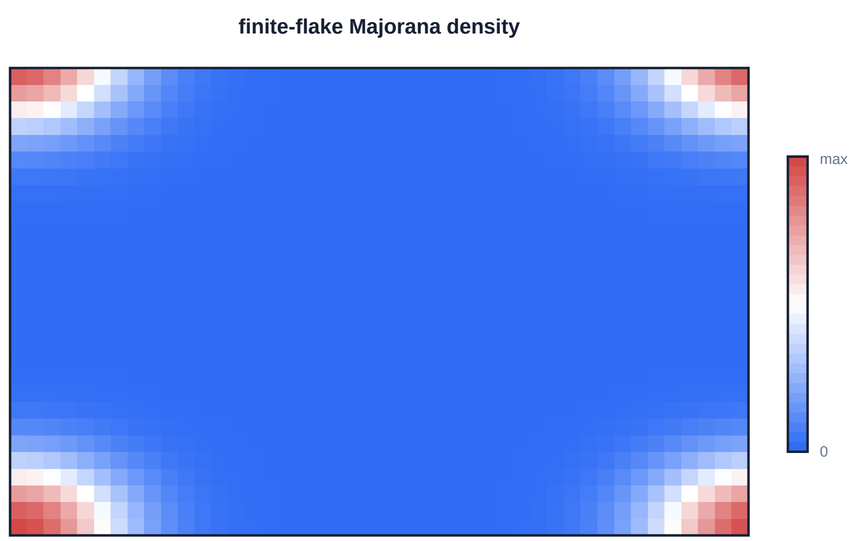

Figure 18: Synthetic finite-flake Majorana density. The finite-device calculation must distinguish topological modes from trivial Andreev bound states by size scaling and particle-hole structure.

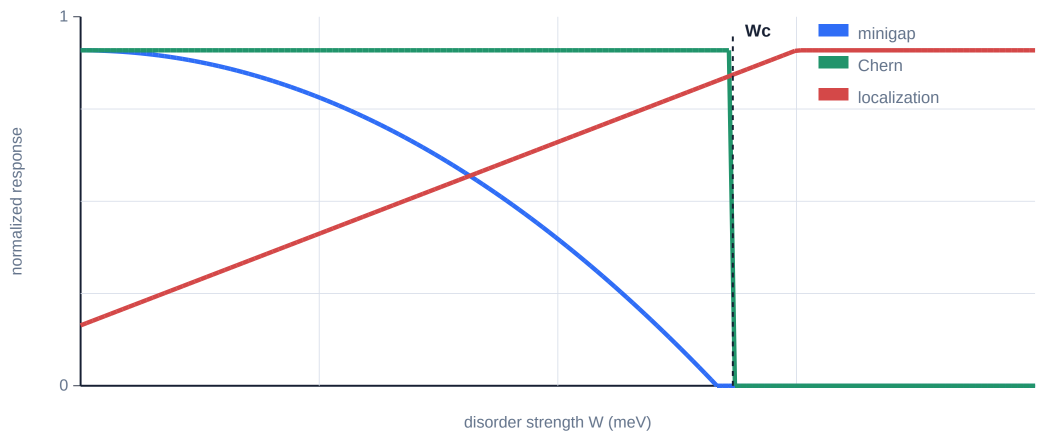

Figure 19: Synthetic robustness curves. The disorder threshold W_c should be extracted from invariant, gap, localization, and finite-size-splitting trends together.

Table 6: Pairing-model comparison in the synthetic demonstration. The prose around the table discusses computational cost; the table keeps only the decision-relevant differences.

Model	Inputs	Best use	Main risk
Constant gap	One scalar pairing scale	Early scans of symmetry and topology	Can overestimate the gap on weakly proximitized topological states.
Band-resolved gap	One value for each Fermi-surface sheet	Multiband systems with weak angular anisotropy	Misses hot spots, cold spots, and sign-changing structure.
Momentum-resolved EPW gap	Anisotropic $\Delta_n(\mathbf{k}, T)$ on dense meshes	Final candidates and quantitative minigap estimates	Expensive and sensitive to interpolation quality.
Layer-resolved proximity	Pairing assigned by orbital or layer weight	Large heterostructures where full EPW is prohibitive	Requires calibrated interface transparency.

Table 7: Experimental observables and control tests. The table is shortened to keep the reader's focus on falsifiable measurements.

Observable	Topology-sensitive response	Control test against trivial explanations
Polarization-dependent zero-bias feature	Edge, corner, or domain-wall spectral weight switches with P	Check nonlocal response, size scaling, and gap closing/re-opening.
Chirality reversal	Edge propagation or thermal/Hall response changes sign below T_c	Compare with normal-state Hall changes above T_c.
Written domain-wall channel	Conducting channel follows the boundary between opposite polar domains	Move or erase the wall electrically and track the channel.
QPI change	Spin-orbit and gap-anisotropy fingerprints reorganize with P	Compare against calculated spin-resolved selection rules.
Josephson anomaly	Current-phase relation reflects a topological boundary channel	Vary transparency, phase bias, and magnetic field independently.

trivial pockets while weak pairing occurs on topological pockets, when the gap has nodes or deep minima near Berry-curvature hot spots, or when interband pairing and spin-orbit texture produce nontrivial singlet-triplet mixing.

18 Experimental Signatures

The proposed device in Fig. 20 uses electrical control of the polar layer and spectroscopic access to edges, corners, or domain walls. Falsifiable signatures should be stated in pairs: the expected topological signal and a trivial alternative explanation.

The strongest experimental test is a sequence: switch P, observe a superconducting gap closing and reopening, detect a corresponding change in edge or domain-wall spectral weight, and verify a chirality or nonlocal transport signature. A zero-bias peak alone is not enough.

19 Validation and Falsification

A serious computational paper must say how it can fail. The TopoEliashberg workflow is falsified for a candidate if the relaxed stack is unstable, the magnetic order is not altermagnetic, the Wannier model fails to reproduce QE bands, phonons show imaginary modes, EPW pairing is too weak or concentrated on trivial bands, the BdG invariant is not converged, or the topological phase exists only at unrealistic chemical potential.

Convergence tests should cover k mesh, q mesh, plane-wave cutoff, vacuum, smearing, Wannier windows, broadening, finite size, disorder realizations, U, and μ^*. The final result should be a convergence matrix, not a sentence claiming convergence.

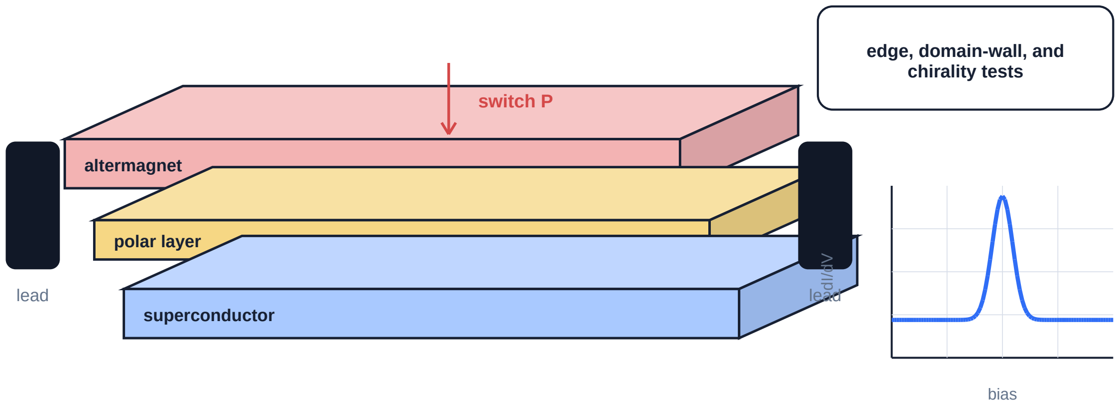

Figure 20: Device schematic and measured zero-bias response. The conductance curve is synthetic. A real device should test chirality, nonlocality, domain-wall localization, and gap closing/reopening.

Table 8: Falsification tests and required response. Short labels keep the table readable while preserving the audit logic.

Failure mode	Diagnostic test	Required response
Wannier error	QE and Wannier bands disagree near E_F	Rebuild projections and windows before any BdG claim.
Imaginary phonons	Negative ω^2 appears in DFPT	Reject the structure or relax a lower-symmetry phase.
Pairing mismatch	Low ETO and weak induced gap on topological bands	Treat constant-gap predictions as unreliable.
Unrealistic tuning	Topology requires impractical gating or doping	Downgrade the result to model interest.
U sensitivity	Topology changes across plausible U values	Report uncertainty and seek calibration.
Disorder fragility	W_c is below estimated interface fluctuations	Do not claim a robust Majorana platform.
Descriptor failure	ETO fails to correlate with minigap trends	Report the counterexample and revise the descriptor.

Table 9: Reproducibility chain and provenance labels. The table is intentionally compact; the detailed templates are included in the appendices.

Stage	Main tools or files	Status in this package
Structure and magnetism	`pw.x`; SCF, relaxation, noncollinear SOC templates	Input templates only; no production QE calculation is claimed.
Wannierization and normal-state topology	`pw2wannier90.x`, Wannier90, Berry-property workflows	Methodology and templates; no material-specific Wannier model is claimed.
Phonons and electron-phonon coupling	`ph.x`, `q2r.x`, `matdyn.x`, EPW	Synthetic reporting figures plus EPW input template.
BdG topology and finite devices	Custom Python/WannierTools-like and Kwant-like solvers	Skeleton code and synthetic model figures; no transport run is claimed.
Provenance record	`COMPLETED_VS_PROPOSED.md`	Separates generated artifacts from proposed future computations.

20 Reproducibility

The repository package accompanying this PDF contains QE, Wannier90, EPW, and BdG skeleton inputs under `inputs/` and `code/`. Table 9 summarizes the computational chain.

The `COMPLETED_VS_PROPOSED.md` file is part of the reproducibility record. It states plainly which artifacts were produced and which physics calculations remain future work.

21 Limitations

The main limitation is computational cost. Full anisotropic EPW on a large vdW heterostructure is expensive because it requires dense electron and phonon meshes, accurate Wannier interpolation, and careful broadening. A second limitation is the treatment of Coulomb repulsion and unconventional pairing. Migdal-Eliashberg theory is appropriate for electron-phonon-mediated superconductors within its domain of validity; it is not a general theory of strongly correlated unconventional superconductivity.

A third limitation is the difficulty of transforming band-resolved EPW gaps into a smooth orbital-spin pairing matrix when bands are entangled and degenerate. This is not a cosmetic issue. A noisy gauge can create artificial nodes or break particle-hole symmetry in the BdG Hamiltonian. A fourth limitation is that a computed clean topological invariant does not guarantee an experimentally useful platform. Disorder, finite temperature, quasiparticle poisoning, and device fabrication can dominate.

22 Future Directions

The immediate next step is to perform actual first-principles screening on a small set of stacks: CrSBr-like vdW altermagnet/sliding hBN/$NbSe_2$, a stronger-polarity Janus-layer variant, and a benchmark non-vdW altermagnet/thin-film-superconductor interface. Each should be run through relaxation, magnetic ordering, SOC bands, Wannier validation, phonons, and at least isotropic electron-phonon calculations before anisotropic EPW is attempted.

A second direction is to automate the ETO/EQG calculation directly from Wannier90 and EPW outputs. The descriptor should be tested on cases where constant-gap models are known to work and cases where they fail. A third direction is to integrate real-space disorder and domain-wall simulations into the same repository so that the transition from first-principles inputs to finite-device predictions is auditable.

23 Conclusion

TopoEliashberg is a first-principles-to-BdG framework for evaluating switchable Majorana phases without hiding the superconducting gap behind a scalar parameter. It assigns each computational responsibility to the correct layer: QE for structure, magnetism, SOC electronic structure, phonons, and electron-phonon ingredients; Wannier90 for spinor Hamiltonians and Berry quantities; EPW for anisotropic pairing; and downstream BdG, Green-function, and finite-device solvers for topology and Majorana diagnostics.

The paper's central technical contribution is the explicit pairing-transfer interface from $\Delta_n(\mathbf{k}, T)$ to $\Delta_{\alpha\beta}(\mathbf{k}, T)$, including gauge and antisymmetry checks. Its central screening idea is the Eliashberg-Topology Overlap and quantum-geometric extensions. Its main scientific target is electrically switchable topological superconductivity in altermagnetic vdW heterostructures, especially phases in which polar reversal changes the BdG Chern number or reverses Majorana chirality. The package deliberately labels all model-generated figures as such. That honesty is not a weakness; it is the condition that makes the proposed workflow reproducible and falsifiable.

A Representative QE SCF Input

Listing 1: Representative `pw.x` SCF input template.

```
&control
  calculation = 'scf',
  prefix = 'am_fe_sc',
  pseudo_dir = './pseudo',
  outdir = './tmp',
  tstress = .true.,
  tprnfor = .true.
/
&system
  ibrav = 0,
  nat = NAT_PLACEHOLDER,
  ntyp = NTYP_PLACEHOLDER,
  ecutwfc = 80.0,
  ecutrho = 640.0,
  occupations = 'smearing',
  smearing = 'mv',
  degauss = 0.015,
  input_dft = 'PBE',
  assume_isolated = '2D'
/
&electrons
  conv_thr = 1.0d-10,
  mixing_beta = 0.25,
  electron_maxstep = 200
/
ATOMIC_SPECIES
  Cr  51.996  Cr.rel-pbe-spn-kjpaw_psl.1.0.0.UPF
  S   32.065  S.rel-pbe-n-kjpaw_psl.1.0.0.UPF
  Br  79.904  Br.rel-pbe-dn-kjpaw_psl.1.0.0.UPF
  B   10.811  B.rel-pbe-n-kjpaw_psl.1.0.0.UPF
  N   14.007  N.rel-pbe-n-kjpaw_psl.1.0.0.UPF
  Nb  92.906  Nb.rel-pbe-spn-kjpaw_psl.1.0.0.UPF
  Se  78.960  Se.rel-pbe-dn-kjpaw_psl.1.0.0.UPF
CELL_PARAMETERS angstrom
  A1X A1Y 0.000
  A2X A2Y 0.000
  0.000 0.000 28.000
ATOMIC_POSITIONS crystal
  ... coordinates from relaxed stack ...
K_POINTS automatic
  12 12 1 0 0 0
```

B Representative QE Relaxation Input

Listing 2: Representative `pw.x` relaxation input template.

```
&control
  calculation = 'relax',
  prefix = 'am_fe_sc',
  pseudo_dir = './pseudo',
  outdir = './tmp',
  tstress = .true.,
  tprnfor = .true.,
  forc_conv_thr = 1.0d-4,
  etot_conv_thr = 1.0d-6
/
&system
  ibrav = 0,
  nat = NAT_PLACEHOLDER,
  ntyp = NTYP_PLACEHOLDER,
  ecutwfc = 80.0,
  ecutrho = 640.0,
  occupations = 'smearing',
```

```
  smearing = 'mv',
  degauss = 0.015,
  input_dft = 'PBE',
  vdw_corr = 'grimme-d3',
  assume_isolated = '2D'
/
&electrons
  conv_thr = 1.0d-10,
  mixing_beta = 0.25
/
&ions
  ion_dynamics = 'bfgs'
/
CELL_PARAMETERS angstrom
  A1X A1Y 0.000
  A2X A2Y 0.000
  0.000 0.000 28.000
ATOMIC_POSITIONS crystal
  ... initial stack coordinates ...
K_POINTS automatic
  8 8 1 0 0 0
```

C Representative SOC NSCF Input

Listing 3: Representative noncollinear spin-orbit NSCF input template.

```
&control
  calculation = 'nscf',
  prefix = 'am_fe_sc',
  pseudo_dir = './pseudo',
  outdir = './tmp'
/
&system
  ibrav = 0,
  nat = NAT_PLACEHOLDER,
  ntyp = NTYP_PLACEHOLDER,
  ecutwfc = 80.0,
  ecutrho = 640.0,
  noncolin = .true.,
  lspinorb = .true.,
  starting_spin_angle = .true.,
  occupations = 'smearing',
  smearing = 'mv',
  degauss = 0.010
/
&electrons
  conv_thr = 1.0d-12
/
K_POINTS crystal
  NK_FINE
  ... uniform or symmetry-reduced fine mesh ...
```

D Representative DFPT Phonon Input

Listing 4: Representative `ph.x` input template.

```
&inputph
  prefix = 'am_fe_sc',
  outdir = './tmp',
  fildyn = 'am_fe_sc.dyn',
  tr2_ph = 1.0d-16,
  ldisp = .true.,
  nq1 = 4, nq2 = 4, nq3 = 1,
  electron_phonon = 'interpolated',
```

```
  fildvscf = 'dvscf'
/
```

E Representative Wannier90 Input

Listing 5: Representative spinor Wannier90 `.win` file.

```
num_wann = 84
num_bands = 132
spinors = true
begin projections
  Cr:d
  S:p
  Br:p
  Nb:d
  Se:p
  B:p
  N:p
end projections
disentanglement = true
dis_win_min = -7.0
dis_win_max =  5.0
dis_froz_min = -1.5
dis_froz_max =  1.5
num_iter = 1000
conv_tol = 1.0d-10
berry = true
berry_task = eval_ahc
berry_kmesh = 200 200 1
begin kpoint_path
  G 0.000 0.000 0.000  K 0.333 0.333 0.000
  K 0.333 0.333 0.000  M 0.500 0.000 0.000
  M 0.500 0.000 0.000  G 0.000 0.000 0.000
end kpoint_path
```

F Representative EPW Input

Listing 6: Representative anisotropic EPW input template.

```
&inputepw
  prefix = 'am_fe_sc'
  outdir = './tmp'
  dvscf_dir = './save'
  elph = .true.
  epbwrite = .true.
  epbread = .false.
  epwwrite = .true.
  epwread = .false.
  wannierize = .true.
  nbndsub = 84
  bands_skipped = 'exclude_bands = 1:20'
  num_iter = 500
  dis_win_min = -7.0
  dis_win_max = 5.0
  dis_froz_min = -1.5
  dis_froz_max = 1.5
  proj = 'Cr:d;S:p;Br:p;Nb:d;Se:p;B:p;N:p'
  wdata(1) = 'spinors = true'
  nk1 = 12, nk2 = 12, nk3 = 1
  nq1 = 4,  nq2 = 4,  nq3 = 1
  mp_mesh_k = .true.
  nkf1 = 120, nkf2 = 120, nkf3 = 1
  nqf1 = 60,  nqf2 = 60,  nqf3 = 1
  eliashberg = .true.
```

```
  laniso = .true.
  limag = .true.
  lpade = .true.
  muc = 0.10
  temps = 1.0 2.0 4.0 6.0
  conv_thr_iaxis = 1.0d-5
/
```

G BdG and Chern-Number Skeleton

Listing 7: Skeleton code for Nambu doubling and Fukui-Hatsugai-Suzuki Chern calculation.

```
"""Skeleton for TopoEliashberg BdG and Chern-number calculations.

This file is intentionally a compact reproducibility aid. It omits the
material-specific Wannier90 H(R) parser and EPW gap parser, which should be
replaced by project-tested readers.
"""

import numpy as np


def enforce_antisymmetry(delta_k, delta_minus_k):
    return 0.5 * (delta_k - delta_minus_k.T)


def bdg_hamiltonian(hw_k, hw_minus_k, delta_k, mu):
    n = hw_k.shape[0]
    upper = np.hstack([hw_k - mu * np.eye(n), delta_k])
    lower = np.hstack([delta_k.conj().T, -hw_minus_k.T + mu * np.eye(n)])
    return np.vstack([upper, lower])


def link_variable(vecs_a, vecs_b):
    overlap = np.linalg.det(vecs_a.conj().T @ vecs_b)
    return overlap / abs(overlap)


def fhs_chern(occupied_eigenvectors):
    """Fukui-Hatsugai-Suzuki Chern number on a rectangular k mesh."""
    nx, ny = occupied_eigenvectors.shape[:2]
    total = 0.0
    for ix in range(nx):
        for iy in range(ny):
            u = occupied_eigenvectors[ix, iy]
            ux = occupied_eigenvectors[(ix + 1) % nx, iy]
            uy = occupied_eigenvectors[ix, (iy + 1) % ny]
            uxy = occupied_eigenvectors[(ix + 1) % nx, (iy + 1) % ny]
            U1 = link_variable(u, ux)
            U2 = link_variable(ux, uxy)
            U3 = link_variable(uy, uxy)
            U4 = link_variable(u, uy)
            total += np.angle(U1 * U2 / (U3 * U4))
    return total / (2 * np.pi)
```

H Additional Derivations

Starting from the Nambu spinor

$$\Psi_{\mathbf{k}} = (c_{1\mathbf{k}}, \ldots, c_{N\mathbf{k}}, c^\dagger_{1,-\mathbf{k}}, \ldots, c^\dagger_{N,-\mathbf{k}})^T, \tag{35}$$

the mean-field Hamiltonian is

$$\mathcal{H} = \frac{1}{2}\sum_{\mathbf{k}} \Psi^\dagger_{\mathbf{k}} H_{\mathrm{BdG}}(\mathbf{k}) \Psi_{\mathbf{k}} + \mathrm{const.} \tag{36}$$

Particle-hole symmetry follows from redundancy of the Nambu basis. With τ_i acting in particle-hole space,

$$\Xi = \tau_x \mathcal{K}, \qquad \Xi H_{\mathrm{BdG}}(\mathbf{k}) \Xi^{-1} = -H_{\mathrm{BdG}}(-\mathbf{k}), \tag{37}$$

when Eq. (25) is satisfied. This check should be evaluated numerically as

$$\epsilon_{\mathrm{PHS}} = \max_{\mathbf{k}} \frac{\|\tau_x H^*_{\mathrm{BdG}}(\mathbf{k})\tau_x + H_{\mathrm{BdG}}(-\mathbf{k})\|_F}{\|H_{\mathrm{BdG}}(\mathbf{k})\|_F}. \tag{38}$$

Values above interpolation precision indicate a basis, gauge, or antisymmetry error.

For a discrete $N_x \times N_y$ mesh, the occupied eigenvectors are stored as a matrix $V(\mathbf{k})$ whose columns span the negative-energy subspace. The link variables are

$$U_i(\mathbf{k}) = \frac{\det[V^\dagger(\mathbf{k})V(\mathbf{k}+\hat{i})]}{|\det[V^\dagger(\mathbf{k})V(\mathbf{k}+\hat{i})]|}. \tag{39}$$

The lattice Berry flux is

$$F_{12}(\mathbf{k}) = \mathrm{Arg}\left[U_1(\mathbf{k})U_2(\mathbf{k}+\hat{1})U_1^{-1}(\mathbf{k}+\hat{2})U_2^{-1}(\mathbf{k})\right], \tag{40}$$

and $\mathcal{C}_{\mathrm{BdG}} = (2\pi)^{-1}\sum_{\mathbf{k}} F_{12}(\mathbf{k})$. Mesh convergence is checked by repeating the calculation until $\mathcal{C}_{\mathrm{BdG}}$ is integer stable and E_{top} changes below tolerance.

I Convergence Matrix Template

Table 10: Convergence matrix template for a completed TopoEliashberg study.

Parameter	Low setting	Production setting	Acceptance criterion
Wave-function cutoff	60 Ry	80–100 Ry	Band inversion and forces stable.
Charge-density cutoff	480 Ry	640–800 Ry	Total energy change below threshold.
Relaxation mesh	$6 \times 6 \times 1$	$8 \times 8 \times 1$ or higher	Forces below 10^{-4} Ry/bohr.
SOC NSCF mesh	$12 \times 12 \times 1$	$24 \times 24 \times 1$ or higher	Spin splitting and Fermi surface stable.
EPW fine electron mesh	$60 \times 60 \times 1$	$120 \times 120 \times 1$ or higher	λ and $\Delta_n(\mathbf{k})$ stable.
EPW fine phonon mesh	$30 \times 30 \times 1$	$60 \times 60 \times 1$ or higher	$\alpha^2 F$ stable.
Wannier windows	narrow	expanded and frozen-checked	Interpolation error below few meV near E_F.
Chern mesh	101×101	301×301 or adaptive	Integer invariant and gap stable.

Parameter	Low setting	Production setting	Acceptance criterion
Disorder samples	20	200+	Gap distribution stable.
Finite flake size	40 nm	100–500 nm extrapolation	Splitting follows exponential trend.

References

[1] Paolo Giannozzi, Stefano Baroni, Nicola Bonini, Matteo Calandra, Roberto Car, Carlo Cavazzoni, Davide Ceresoli, Guido L. Chiarotti, Matteo Cococcioni, Ismaila Dabo, Andrea Dal Corso, Stefano de Gironcoli, Stefano Fabris, Guido Fratesi, Ralph Gebauer, Uwe Gerstmann, Christos Gougoussis, Anton Kokalj, Michele Lazzeri, Layla Martin-Samos, Nicola Marzari, Francesco Mauri, Riccardo Mazzarello, Stefano Paolini, Alfredo Pasquarello, Lorenzo Paulatto, Carlo Sbraccia, Sandro Scandolo, Gabriele Sclauzero, Ari P. Seitsonen, Alexander Smogunov, Paolo Umari, and Renata M. Wentzcovitch. Quantum espresso: a modular and open-source software project for quantum simulations of materials. *Journal of Physics: Condensed Matter*, 21:395502, 2009. doi: 10.1088/0953-8984/21/39/395502.

[2] Paolo Giannozzi, Oliviero Andreussi, Thomas Brumme, Olivier Bunau, Marco Buongiorno Nardelli, Matteo Calandra, Roberto Car, Carlo Cavazzoni, Davide Ceresoli, Matteo Cococcioni, Nicola Colonna, Ivan Carnimeo, Andrea Dal Corso, Stefano de Gironcoli, Pietro Delugas, Robert A. DiStasio, Andrea Ferretti, Andrea Floris, Guido Fratesi, Giorgia Fugallo, Ralph Gebauer, Uwe Gerstmann, Feliciano Giustino, Tommaso Gorni, Jia Jia, Mitsuaki Kawamura, Hyungjun-Yoon Ko, Anton Kokalj, Emine Kucukbenli, Michele Lazzeri, Margherita Marsili, Nicola Marzari, Francesco Mauri, Nguyen L. Nguyen, Hung-Vu Nguyen, Alberto Otero-de-la Roza, Lorenzo Paulatto, Samuel Ponce, Dario Rocca, Riccardo Sabatini, Biswajit Santra, Martin Schlipf, Ari P. Seitsonen, Alexander Smogunov, Iurii Timrov, Timo Thonhauser, Paolo Umari, Nathalie Vast, Xifan Wu, and Stefano Baroni. Advanced capabilities for materials modelling with quantum espresso. *Journal of Physics: Condensed Matter*, 29:465901, 2017. doi: 10.1088/1361-648X/aa8f79.

[3] Paolo Giannozzi, Oscar Baseggio, Pietro Bonfa, Davide Brunato, Roberto Car, Ivan Carnimeo, Carlo Cavazzoni, Stefano de Gironcoli, Pietro Delugas, Fabrizio Ferrari Ruffino, Andrea Ferretti, Nicola Marzari, Iurii Timrov, Andrea Urru, and Stefano Baroni. Quantum espresso toward the exascale. *Journal of Chemical Physics*, 152:154105, 2020. doi: 10.1063/5.0005082.

[4] Quantum ESPRESSO Foundation. What can qe do, 2026. URL https://www.quantum-espresso.org/what-can-qe-do/. Accessed 2026-07-18.

[5] Quantum ESPRESSO Foundation. pw.x input description, 2026. URL https://www.quantum-espresso.org/Doc/INPUT_PW.html. Accessed 2026-07-18.

[6] Arash A. Mostofi, Jonathan R. Yates, Young-Su Lee, Ivo Souza, David Vanderbilt, and Nicola Marzari. wannier90: A tool for obtaining maximally-localised wannier functions. *Computer Physics Communications*, 178:685–699, 2008. doi: 10.1016/j.cpc.2007.11.016.

[7] Giovanni Pizzi, Valerio Vitale, Ryotaro Arita, Stefan Blugel, Frank Freimuth, Guillaume Geranton, Marco Gibertini, Dominik Gresch, Charles Johnson, Takashi Koretsune, Julen Ibañez-Azpiroz, Hyungjun Lee, Jae-Mo Lihm, Dominique Marchand, Antimo Marrazzo, Yuriy Mokrousov, Jamal I. Mustafa, Yoshiro Nohara, Yusuke Nomura, Lorenzo Paulatto, Samuel Ponce, Thomas Ponweiser,

Junfeng Qiao, Florian Thole, Stepan S. Tsirkin, Malgorzata Wierzbowska, Nicola Marzari, David Vanderbilt, Ivo Souza, Arash A. Mostofi, and Jonathan R. Yates. Wannier90 as a community code: new features and applications. *Journal of Physics: Condensed Matter*, 32:165902, 2020. doi: 10.1088/1361-648X/ab51ff.

[8] Wannier90 Developers. Wannier90 features and berry-property tutorials, 2026. URL https://wannier.org/features/. Accessed 2026-07-18.

[9] S. Ponce, E. R. Margine, C. Verdi, and F. Giustino. Epw: Electron-phonon coupling, transport and superconducting properties using maximally localized wannier functions. *Computer Physics Communications*, 209:116–133, 2016. doi: 10.1016/j.cpc.2016.07.028.

[10] E. R. Margine and F. Giustino. Anisotropic migdal-eliashberg theory using wannier functions. *Physical Review B*, 87:024505, 2013. doi: 10.1103/PhysRevB.87.024505.

[11] EPW Code Developers. Migdal-eliashberg theory and superconducting-property documentation, 2026. URL https://docs.epw-code.org/. Accessed 2026-07-18.

[12] Libor Smejkal, Jairo Sinova, and Tomas Jungwirth. Beyond conventional ferromagnetism and antiferromagnetism: A phase with nonrelativistic spin and crystal rotation symmetry. *Physical Review X*, 12:031042, 2022. doi: 10.1103/PhysRevX.12.031042.

[13] Libor Smejkal, Jairo Sinova, and Tomas Jungwirth. Emerging research landscape of altermagnetism. *Physical Review X*, 12:040501, 2022. doi: 10.1103/PhysRevX.12.040501.

[14] Cheng Song, Hua Bai, Zhiyuan Zhou, Lei Han, Helena Reichlova, J. Hugo Dil, J. Liu, X. Chen, and F. Pan. Altermagnets as a new class of functional materials. *Nature Reviews Materials*, 10:473, 2025. doi: 10.1038/s41578-025-00779-1.

[15] Sayed Ali Akbar Ghorashi, Taylor L. Hughes, and Jennifer Cano. Altermagnetic routes to majorana modes in zero net magnetization. *Physical Review Letters*, 133:106601, 2024. doi: 10.1103/PhysRevLett.133.106601.

[16] Andreas Hadjipaschalis, Sayed Ali Akbar Ghorashi, and Jennifer Cano. Majoranas with a twist: Tunable majorana zero modes in altermagnetic heterostructures. *Physical Review B*, 112:214430, 2025. doi: 10.1103/p79l-rty6.

[17] Ziye Zhu, Richang Huang, Xianzhang Chen, Zhou Cui, Xunkai Duan, Jiayong Zhang, Igor Zutic, and Tong Zhou. Altermagnetic proximity effect. *Physical Review Letters*, 136:186702, 2026. doi: 10.1103/kqy8-myz1.

[18] M. Vizner Stern, Y. Waschitz, W. Cao, I. Nevo, K. Watanabe, T. Taniguchi, E. Sela, M. Urbakh, O. Hod, and M. Ben Shalom. Interfacial ferroelectricity by van der waals sliding. *Science*, 372: 1462–1466, 2021. doi: 10.1126/science.abe8177.

[19] Xiaoming Zhang, Pei Zhao, and Feng Liu. Ferroelectric topological superconductor: alpha-in2se3. *Physical Review B*, 109:125130, 2024. doi: 10.1103/PhysRevB.109.125130.

[20] Kai-Zhi Bai, Bo Fu, and Shun-Qing Shen. Ferroelectrically switchable chirality in topological superconductivity. *Physical Review B*, 112:104509, 2025. doi: 10.1103/9jg5-7rk5.

[21] L. Craco and S. S. Carara. Theory of interlayer coupling in crsbr altermagnet semiconductor. *European Physical Journal B*, 98:220, 2025. doi: 10.1140/epjb/s10051-025-01071-5.

[22] Xiaoxiang Xi, Zefang Wang, Weiwei Zhao, Ju-Hyun Park, Kam Tuen Law, Helmuth Berger, Laszlo Forro, Jie Shan, and Kin Fai Mak. Ising pairing in superconducting nbse2 atomic layers. *Nature Physics*, 12:139–143, 2016. doi: 10.1038/nphys3538.

[23] A. Yu. Kitaev. Unpaired majorana fermions in quantum wires. *Physics-Uspekhi*, 44:131–136, 2001. doi: 10.1070/1063-7869/44/10S/S29.

[24] N. Read and Dmitry Green. Paired states of fermions in two dimensions with breaking of parity and time-reversal symmetries and the fractional quantum hall effect. *Physical Review B*, 61:10267–10297, 2000. doi: 10.1103/PhysRevB.61.10267.

[25] Andreas P. Schnyder, Shinsei Ryu, Akira Furusaki, and Andreas W. W. Ludwig. Classification of topological insulators and superconductors in three spatial dimensions. *Physical Review B*, 78:195125, 2008. doi: 10.1103/PhysRevB.78.195125.

[26] Alexei Kitaev. Periodic table for topological insulators and superconductors. *AIP Conference Proceedings*, 1134:22–30, 2009. doi: 10.1063/1.3149495.

[27] Shinsei Ryu, Andreas P. Schnyder, Akira Furusaki, and Andreas W. W. Ludwig. Topological insulators and superconductors: tenfold way and dimensional hierarchy. *New Journal of Physics*, 12: 065010, 2010. doi: 10.1088/1367-2630/12/6/065010.

[28] Masatoshi Sato and Yoichi Ando. Topological superconductors: a review. *Reports on Progress in Physics*, 80:076501, 2017. doi: 10.1088/1361-6633/aa6ac7.

[29] Jason Alicea. New directions in the pursuit of majorana fermions in solid state systems. *Reports on Progress in Physics*, 75:076501, 2012. doi: 10.1088/0034-4885/75/7/076501.

[30] C. W. J. Beenakker. Search for majorana fermions in superconductors. *Annual Review of Condensed Matter Physics*, 4:113–136, 2013. doi: 10.1146/annurev-conmatphys-030212-184337.

[31] Liang Fu and C. L. Kane. Superconducting proximity effect and majorana fermions at the surface of a topological insulator. *Physical Review Letters*, 100:096407, 2008. doi: 10.1103/PhysRevLett.100.096407.

[32] Roman M. Lutchyn, Jay D. Sau, and S. Das Sarma. Majorana fermions and a topological phase transition in semiconductor-superconductor heterostructures. *Physical Review Letters*, 105:077001, 2010. doi: 10.1103/PhysRevLett.105.077001.

[33] Yuval Oreg, Gil Refael, and Felix von Oppen. Helical liquids and majorana bound states in quantum wires. *Physical Review Letters*, 105:177002, 2010. doi: 10.1103/PhysRevLett.105.177002.

[34] Themba Hodge, Eric Mascot, and Stephan Rachel. Altermagnet-superconductor heterostructure: A scalable platform for braiding of majorana modes. *APS Open Science*, 1:L000045, 2026. doi: 10.1103/bfwd-hcm5.

[35] M. V. Berry. Quantal phase factors accompanying adiabatic changes. *Proceedings of the Royal Society A*, 392:45–57, 1984. doi: 10.1098/rspa.1984.0023.

[36] D. J. Thouless, M. Kohmoto, M. P. Nightingale, and M. den Nijs. Quantized hall conductance in a two-dimensional periodic potential. *Physical Review Letters*, 49:405–408, 1982. doi: 10.1103/PhysRevLett.49.405.

[37] Yugui Yao, Leonard Kleinman, A. H. MacDonald, Jairo Sinova, Tomas Jungwirth, Ding-sheng Wang, Enge Wang, and Qian Niu. First principles calculation of anomalous hall conductivity in ferromagnetic bcc fe. *Physical Review Letters*, 92:037204, 2004. doi: 10.1103/PhysRevLett.92.037204.

[38] Di Xiao, Ming-Che Chang, and Qian Niu. Berry phase effects on electronic properties. *Reviews of Modern Physics*, 82:1959–2007, 2010. doi: 10.1103/RevModPhys.82.1959.

[39] J. P. Provost and G. Vallee. Riemannian structure on manifolds of quantum states. *Communications in Mathematical Physics*, 76:289–301, 1980. doi: 10.1007/BF02193559.

[40] Sebastiano Peotta and Paivi Torma. Superfluidity in topologically nontrivial flat bands. *Nature Communications*, 6:8944, 2015. doi: 10.1038/ncomms9944.

[41] Long Liang, Tuomas I. Vanhala, Sebastiano Peotta, Topi Siro, Ari Harju, and Paivi Torma. Band geometry, berry curvature, and superfluid weight. *Physical Review B*, 95:024515, 2017. doi: 10.1103/PhysRevB.95.024515.

[42] Stefano Baroni, Stefano de Gironcoli, Andrea Dal Corso, and Paolo Giannozzi. Phonons and related crystal properties from density-functional perturbation theory. *Reviews of Modern Physics*, 73:515–562, 2001. doi: 10.1103/RevModPhys.73.515.

[43] Feliciano Giustino. Electron-phonon interactions from first principles. *Reviews of Modern Physics*, 89:015003, 2017. doi: 10.1103/RevModPhys.89.015003.

[44] W. L. McMillan. Transition temperature of strong-coupled superconductors. *Physical Review*, 167: 331–344, 1968. doi: 10.1103/PhysRev.167.331.

[45] P. B. Allen and R. C. Dynes. Transition temperature of strong-coupled superconductors reanalyzed. *Physical Review B*, 12:905–922, 1975. doi: 10.1103/PhysRevB.12.905.

[46] A. B. Migdal. Interaction between electrons and lattice vibrations in a normal metal. *Soviet Physics JETP*, 7:996–1001, 1958.

[47] G. M. Eliashberg. Interactions between electrons and lattice vibrations in a superconductor. *Soviet Physics JETP*, 11:696–702, 1960.

[48] T. Fukui, Y. Hatsugai, and H. Suzuki. Chern numbers in discretized brillouin zone. *Journal of the Physical Society of Japan*, 74:1674–1677, 2005. doi: 10.1143/JPSJ.74.1674.

[49] Terry A. Loring and Matthew B. Hastings. Disordered topological insulators via c*-algebras. *Europhysics Letters*, 92:67004, 2010. doi: 10.1209/0295-5075/92/67004.

[50] Raffaello Bianco and Raffaele Resta. Mapping topological order in coordinate space. *Physical Review Letters*, 110:087202, 2013. doi: 10.1103/PhysRevLett.110.087202.

[51] C. W. Groth, M. Wimmer, A. R. Akhmerov, and X. Waintal. Kwant: a software package for quantum transport. *New Journal of Physics*, 16:063065, 2014. doi: 10.1088/1367-2630/16/6/063065.